National Aeronautics and Space Administration

An Improved Plant Nitrogen Cycle in the Community Land Model

Principal Investigator: Mingjie Shi[1] (329C)
Co-I: Joshua B. Fisher[1] (329C)
Edward R. Brzostek[2], Richard P. Phillips[3]

1. INTRODUCTION

Background:

- Plants typically expend a significant portion of their available carbon (C) for nitrogen (N) acquisition.
- Most global terrestrial biosphere models do not consider the C cost for N acquisition.

Scientific Questions:

1. How much N is taken up and what is the global distribution?
2. How does the C cost of N acquisition vary spatially and temporally?
3. How sensitive is the land C sink to a dynamic prediction of the C cost of N acquisition?

2. MODELING APPROACH

The Fixation and Uptake of Nitrogen (FUN) model was coupled into the Community Land Model (CLM) version 4.0.

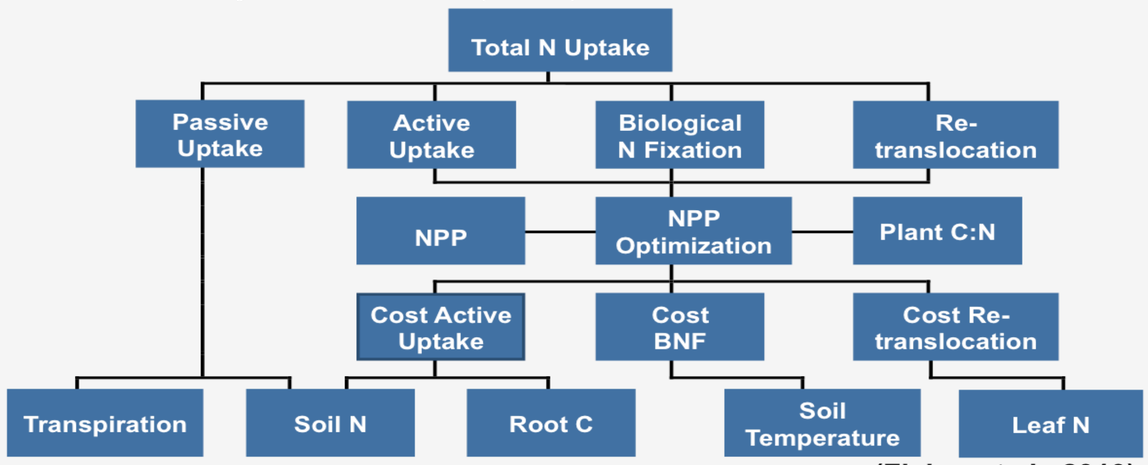

(Fisher et al., 2010)

CLM provides FUN:

1) Available C	2) Soil mineral N	3) Root Biomass
4) Leaf N	5) Plant C:N ratio	6) Soil layer depth
7) Soil temperature	8) Transpiration	

4. N ACQUISITION AND C COST BY BIOME

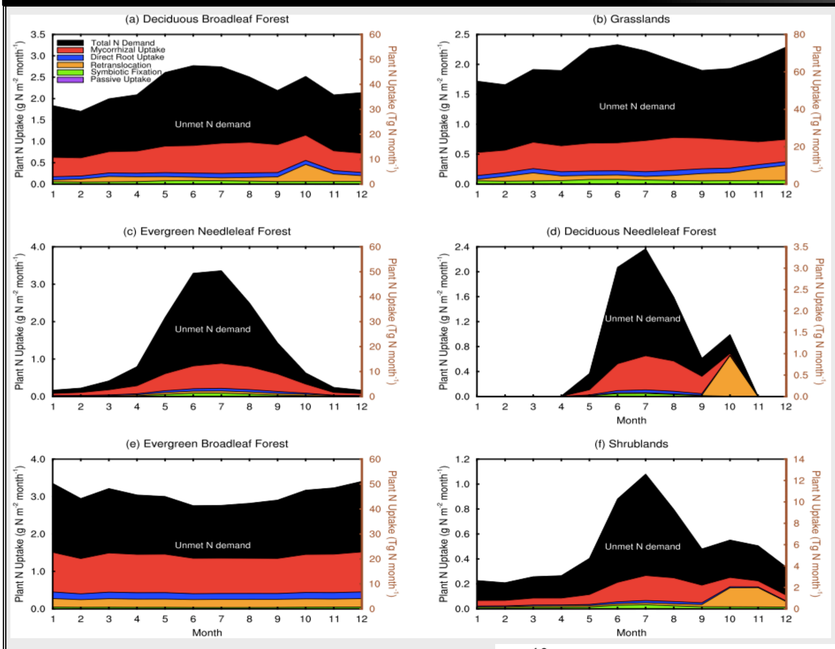

Total N uptake does not meet total N demand for most of the year in all biomes.

Evergreen broadleaf forest has the largest N uptake rate.

Evergreen broadleaf forest has the most unmet demand; shrubland has the most met demand.

C spent on N acquisition is 2.4 Pg C yr^{-1} globally.

The mycorrhizal root uptake and retranslocation used C amounts are 1.2 Pg C yr^{-1} and 0.6 Pg C yr^{-1}, respectively.

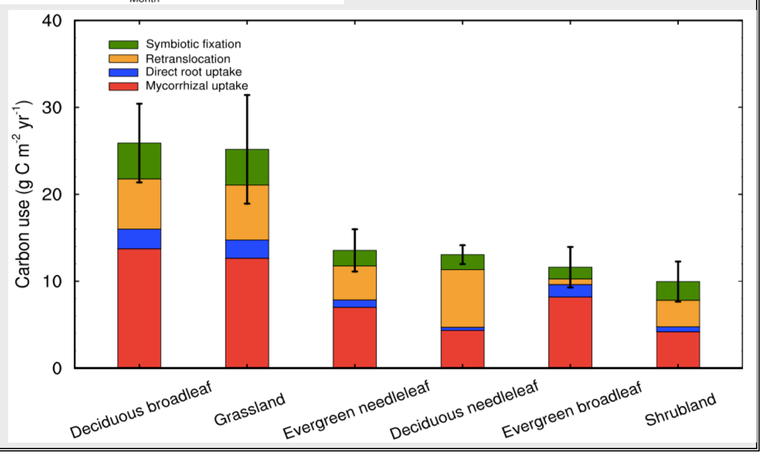

3. N TAKEN UP AND THE GLOBAL DISTRIBUTION?

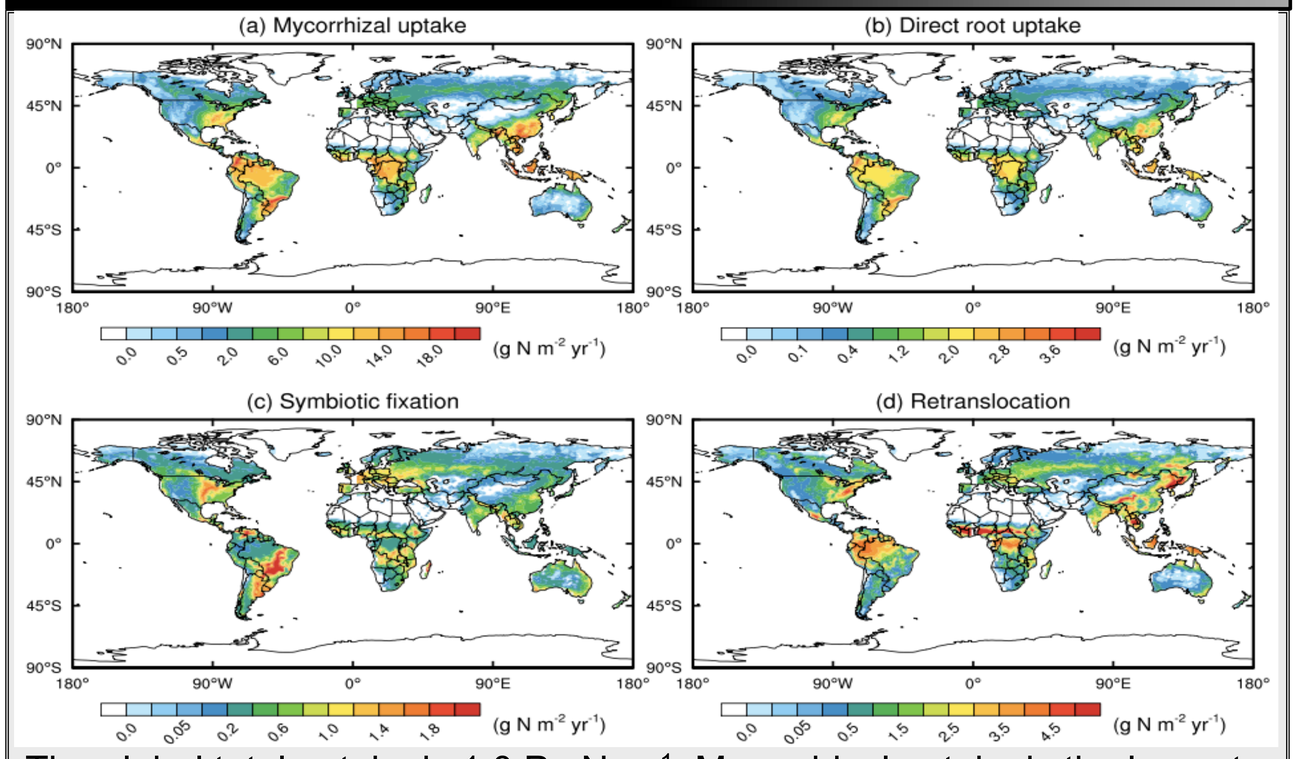

The global total uptake is 1.0 Pg N yr^{-1}. Mycorrhizal uptake is the largest uptake pathway, followed by retranslocation, direct root uptake, and fixation.

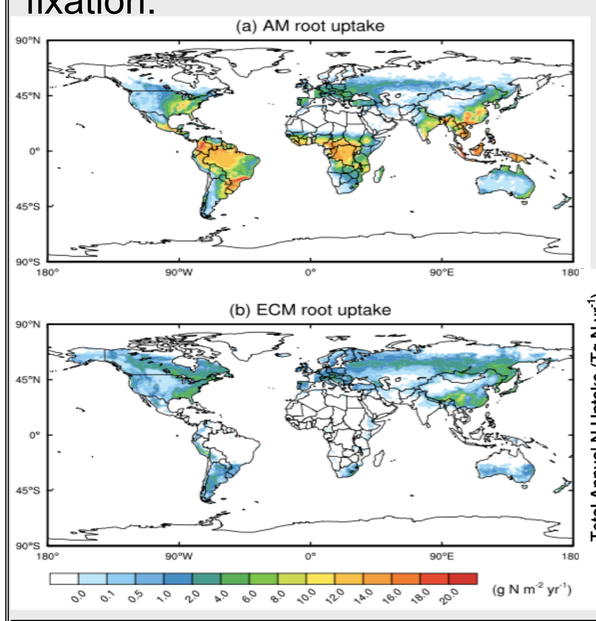

AM fungal uptake exceeds ECM fungal uptake globally.

The AM and ECM uptake is 82% and 18% of the total mycorrhizal uptake, respectively.

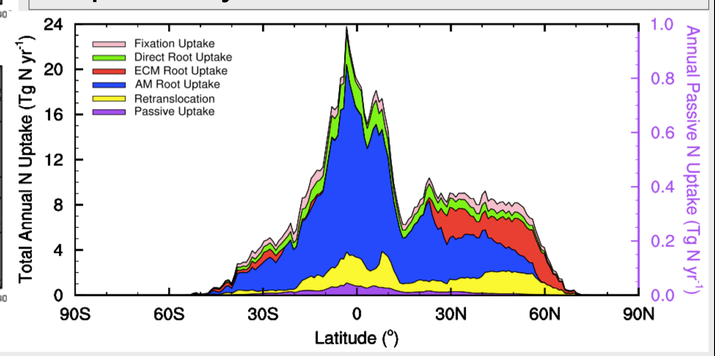

5. C USE AND NPP DOWNREGULATION

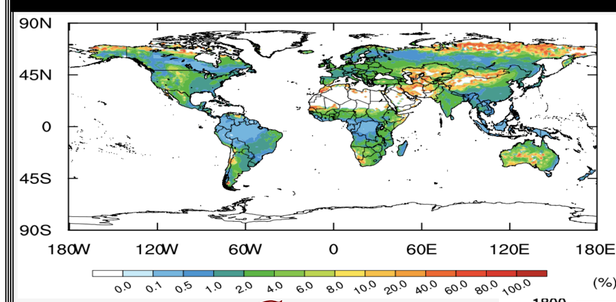

Tropical forests have the lowest C use ratio.

High-latitude shrubland and arid and semi-arid regions have the highest C use ratio.

$$C_{use.ratio} = \frac{C_{use,\ acquisition}}{C_{available}}$$

Global total NPP is down-regulated by 13% globally. The reduced NPP amount peaks at 2°S.

6. CONCLUSIONS

- Global total N uptake amount is 1.0 Pg N yr^{-1}.
- N acquisition uses 2.4 Pg C yr^{-1} globally.
- Mycorrhizal N uptake is the dominant N uptake and the most expensive N uptake pathway.
- Total N uptake reduces NPP globally by 13%.

National Aeronautics and Space Administration
Jet Propulsion Laboratory
California Institute of Technology
Pasadena, California

www.nasa.gov

Acknowledgments. This research was funded by the US Department of Energy Office of Biological and Environmental Research Terrestrial Ecosystem Science Program and the US National Science Foundation Ecosystem Science Program.

1 Jet Propulsion Laboratory, California Institute of Technology; 2 Department of Biology, West Virginia University; 3 Department of Biology, Indiana University

Poster No. EB-1

National Aeronautics and Space Administration

LA Megacity: An Integrated Land-Atmosphere System For Urban CO_2 Emissions

Principal Investigator: Sha Feng (329L)

Thomas Lauvaux (329L), Clare Wong (329J), Meemong Lee (329L), Junjie Liu (329L), Zhijin Li (329D), Riley Duren (8000), Charles E. Miller (3290)

1. GREENHOUSE GAS MODELING FRAMEWORK

OBJECTIVES: To improve understanding of localized, high-flux elements of the carbon cycle; To support efforts by local stakeholders to evaluate actions intended to stabilize urban GHG emissions.

Scientific questions we want to answer:

- How do the fossil fuel emissions impact CO_2 simulations?
- How do the atmospheric CO_2 fields associated with the LA megacity vary spatially across the complex urban to rural gradient?

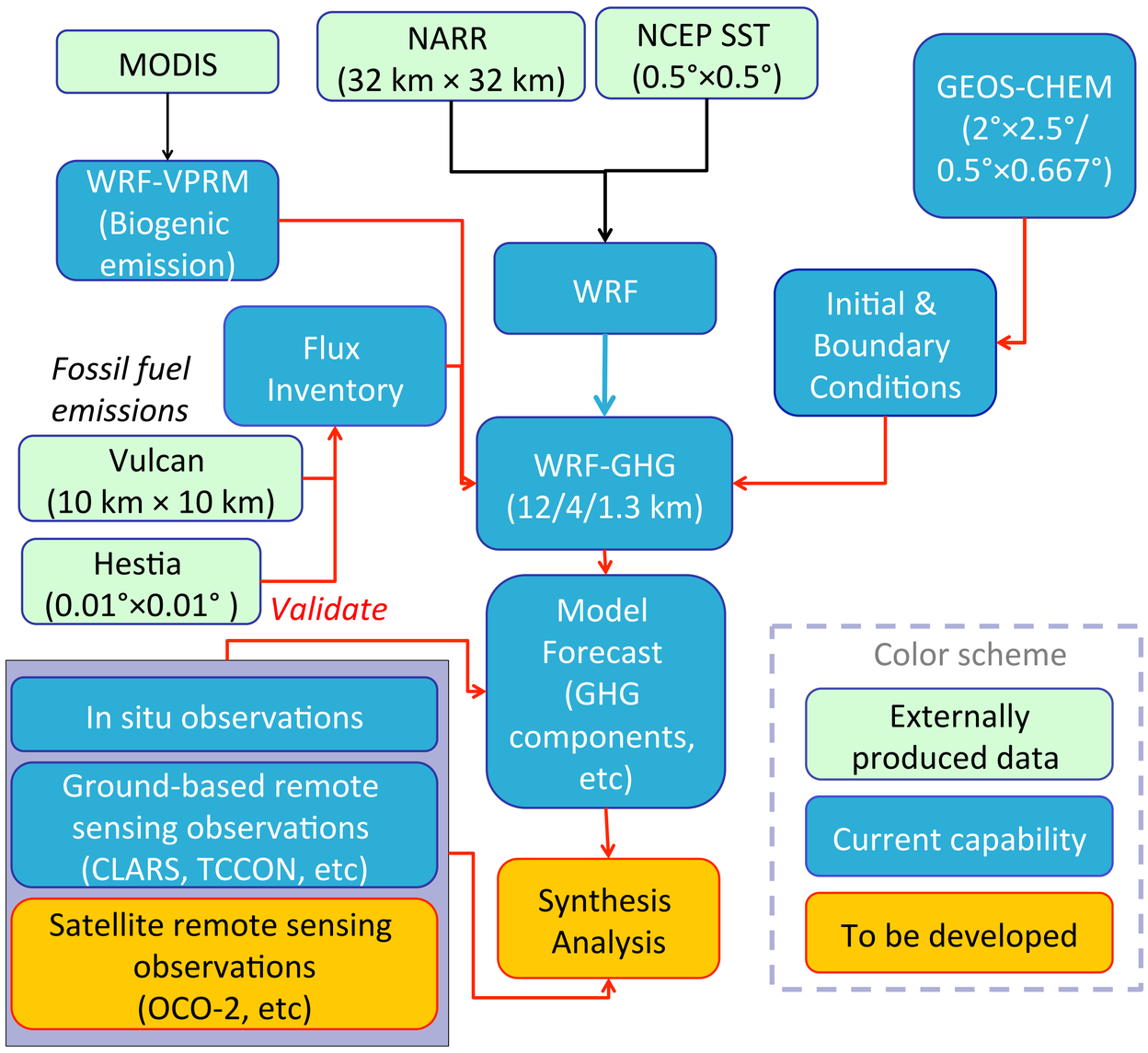

2. MODEL VALIDATION

1. Model vs. Picarro (In situ observations)

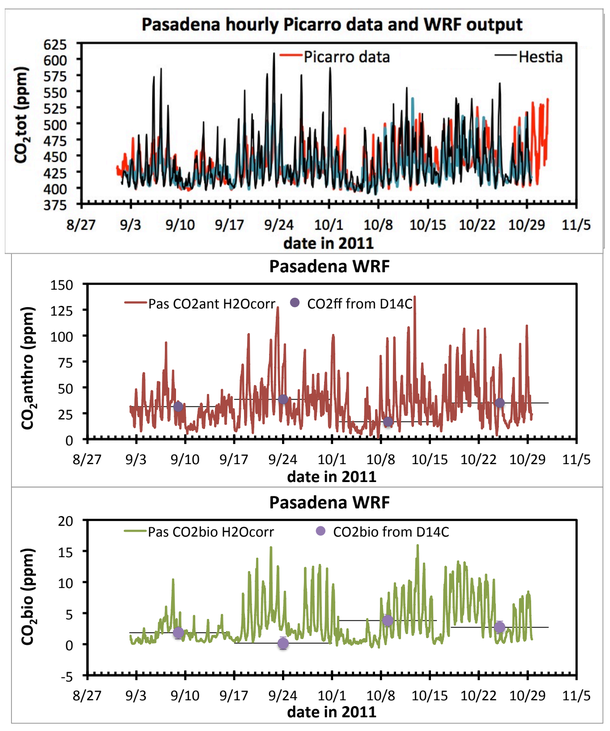

- Model overall performed reasonable job on the simulation of the total CO_2, anthropogenic CO_2 (~50 ppm on average), and biogenic CO_2 (~5 ppm on average).
- Model driven with Hestia emissions (see poster #EB-6) somewhat overestimated the total CO_2 concentration, especially during the nighttime.

2. Model vs. CLARS (Ground-based remote sensing observations)

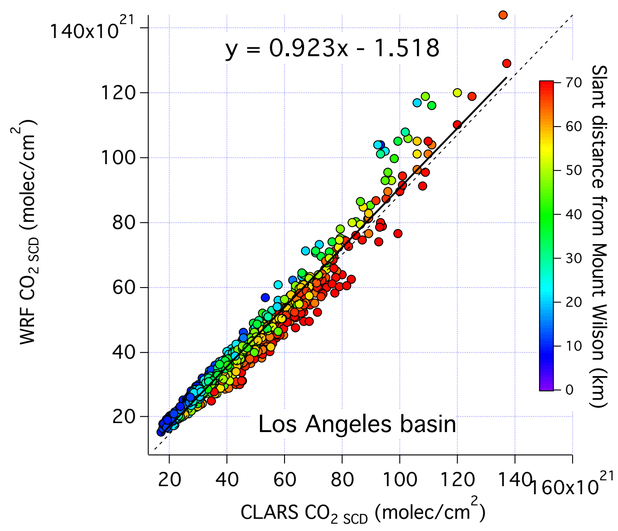

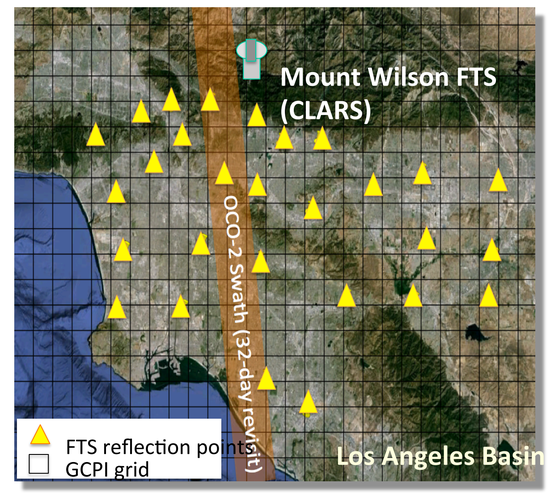

- Modeled column CO_2 correlated well with the CLARS spectralon
- The quality of correlation with the slant column decreased as slant distance became longer than 30 km.

3. RESULTS – URBAN CO_2 DOME

2011-09-27 14:00 LST

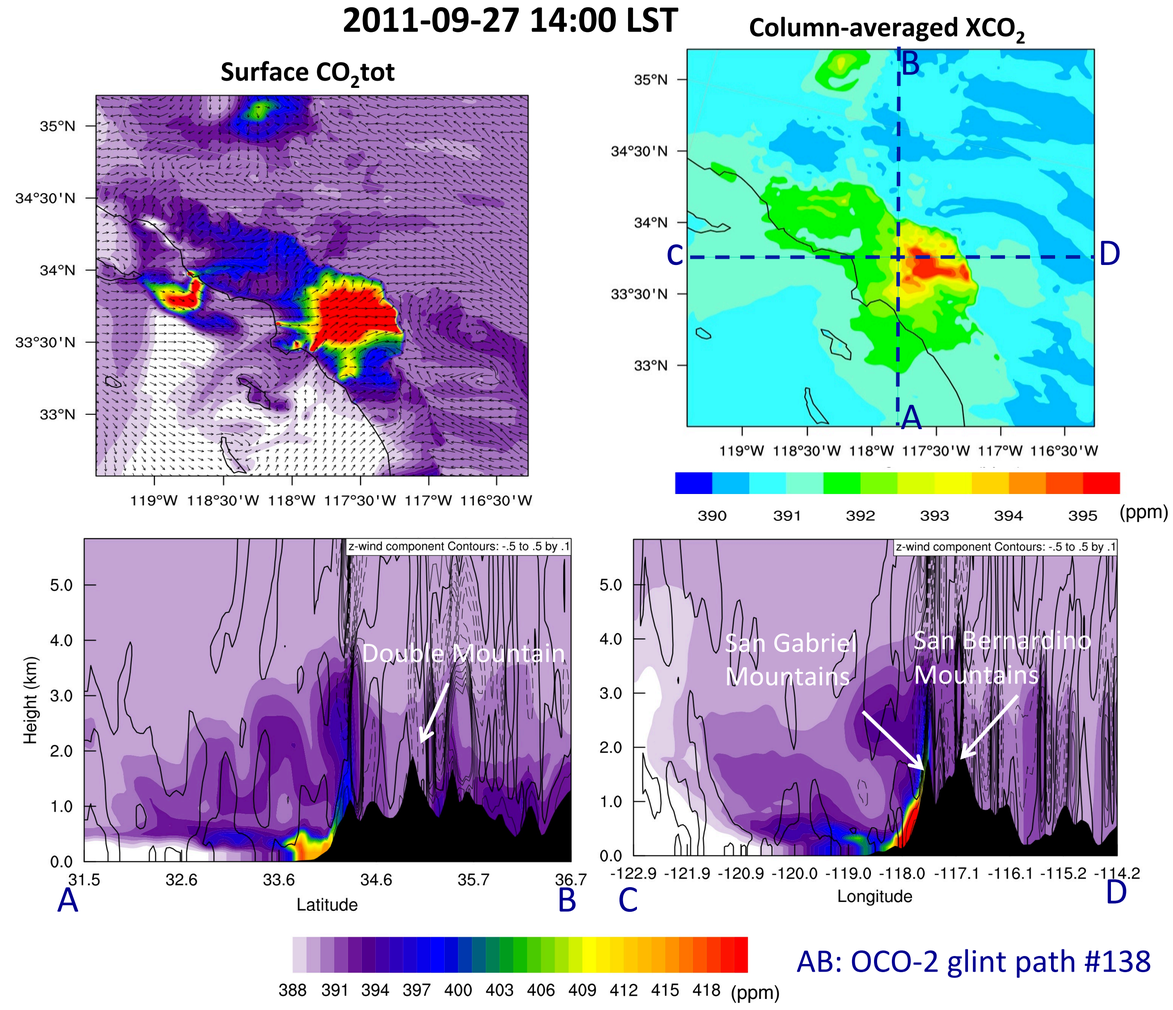

- CO_2 was trapped in the valley as results of sea breeze and mountain blocking even at 2pm.
- Vertical distribution of CO_2 was affected by both orography and vertical circulation.
- Column-averaged XCO_2 varied from 391 ppm to 395 ppm over the LA basin.

4. CONCLUSIONS

- A high-resolution greenhouse gas modeling system was developed to understand the carbon exchange over the Los Angeles megacity.
- The model performs reasonably compared with in-situ and ground-based remote sensing observations.
- Atmospherically transported CO_2 and its surface fluxes are significantly coupled by mesoscale circulation and orography over the LA basin.

Poster No. EB-2

National Aeronautics and Space Administration
Jet Propulsion Laboratory
California Institute of Technology
Pasadena, California
www.nasa.gov

National Aeronautics and Space Administration

Can Land-Ocean Differences of the Warm Rain Formation Process be Explained by Vertical Velocity?

Principal Investigator: Hanii Takahashi (329F)
Kentaro Suzuki (The University of Tokyo) and Graeme Stephens (3292)

1. Introduction

- Warm liquid clouds are of fundamental importance to the global climate since **their cloud-drizzle-rain processes play a key role in controlling the energy budgets and hydrologic cycles.**
- Nakajima et al (2010) and Suzuki et al (2010) introduced a novel methodology called **CFODD** (Contour Frequency by Optical Depth Diagram), **which provides a lifecycle view of warm clouds** to investigate the microphysical processes.

2. Motivation: The land-ocean difference in CFODD

cloud (<-10dBZ) ➔ drizzle (>-10dBZ & <0dBZ) ➔ rain (>0dBZ)

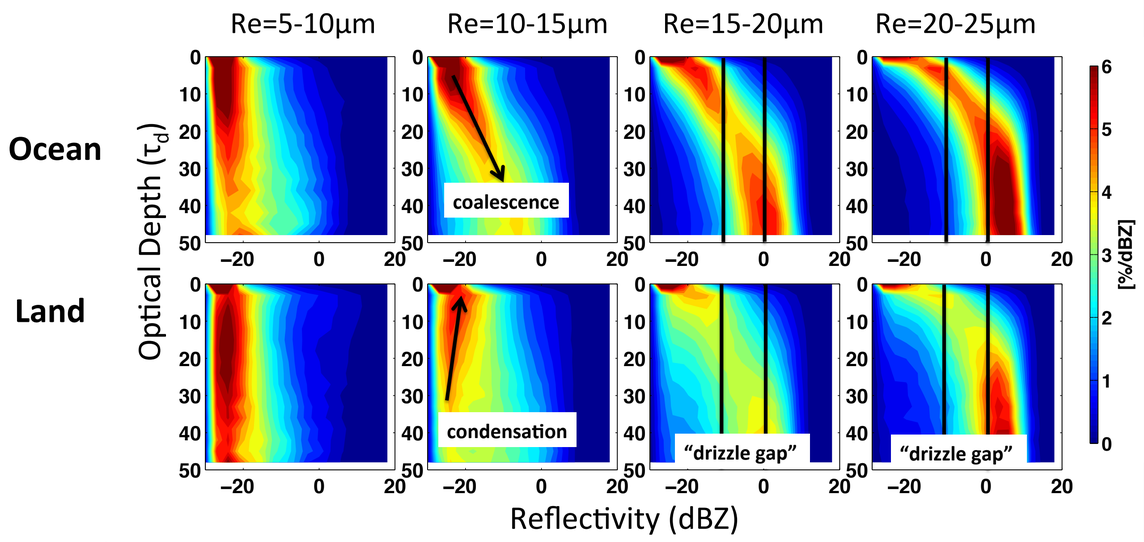

Re: Effective radius

Optical depth:

$$\tau_d(h) = \tau_c\left[1-\left(\frac{h}{H}\right)^{5/3}\right]$$

where τ_c is total optical depth, and H is geometric thickness

- ❖ For Re = 10-15μm, coalescence process starts faster in the oceanic warm clouds.
- ❖ For Re = 15-25μm, "drizzle gap" can be seen over land (drizzle suppression).

Hypothesis: The land-ocean differences are due to the land-ocean differences in the intensity of updraft.

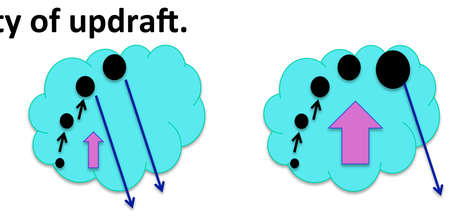

weaker updraft (i.e., ocean) **stronger updraft (i.e., land)**

- Nakajima et al (2010) hypothesized that land-ocean differences in drizzle might be explained by land-ocean differences in updraft strengths. **However, how vertical velocity affects the cloud-drizzle-rain formation process has not yet been tested.**

3. Objective

- **This study examines the land-ocean difference in the warm rain formation process** using CloudSat and MODIS (Moderate Resolution Imaging Spectroradiometer) satellite observations.
- Atmospheric Radiation Measurement (ARM) ground-based data and a 1D model based on spectral-bin microphysics are analyzed **to test how vertical velocity affects the warm rain formation process.**
- This study contributes to **model improvements in warm cloud microphysics at a fundamental process level**, and also **motivates measurement of vertical profiles of cloud microphysical properties and velocity by future satellite missions.**

4. Testing our hypothesis I: A-Train observation (2007-2009)

Oceanic clouds (Re = 15-20μm) sorted by lower tropospheric stability (LTS)

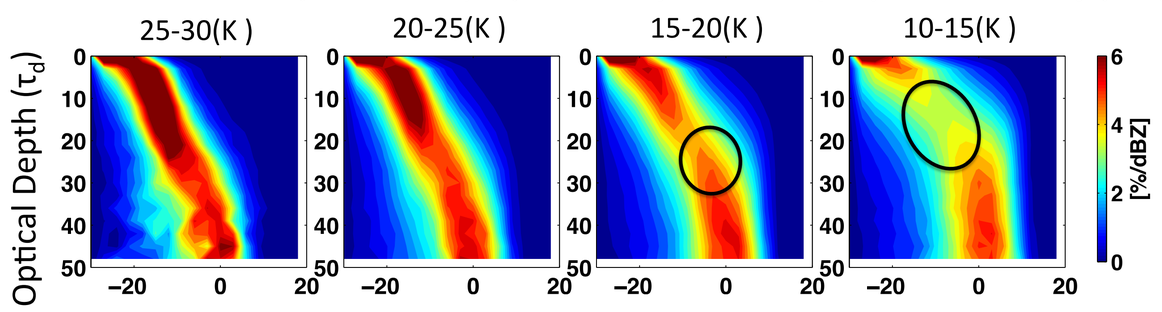

Likely to have weaker updraft (i.e., ocean) ⟷ Likely to have stronger updraft (i.e., land)

❖ **"Drizzle gap" is significant when LTS is lower.**

5. Testing our hypothesis II: ARM observation (2009-2010)

Azores, Portugal (Re = 10-20μm) sorted by vertical velocity (w)

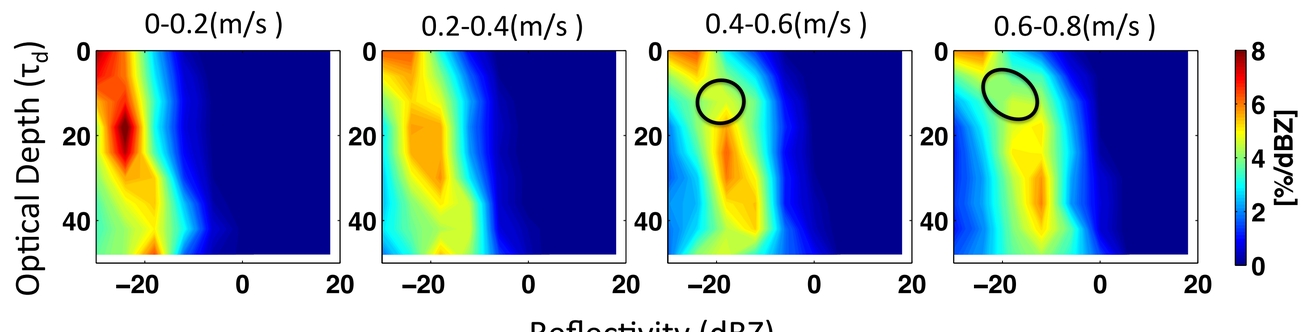

weaker updraft ⟷ stronger updraft

❖ **"Drizzle gap" starts to appear when vertical velocity is stronger.**

6. Testing our hypothesis III: 1D model simulations

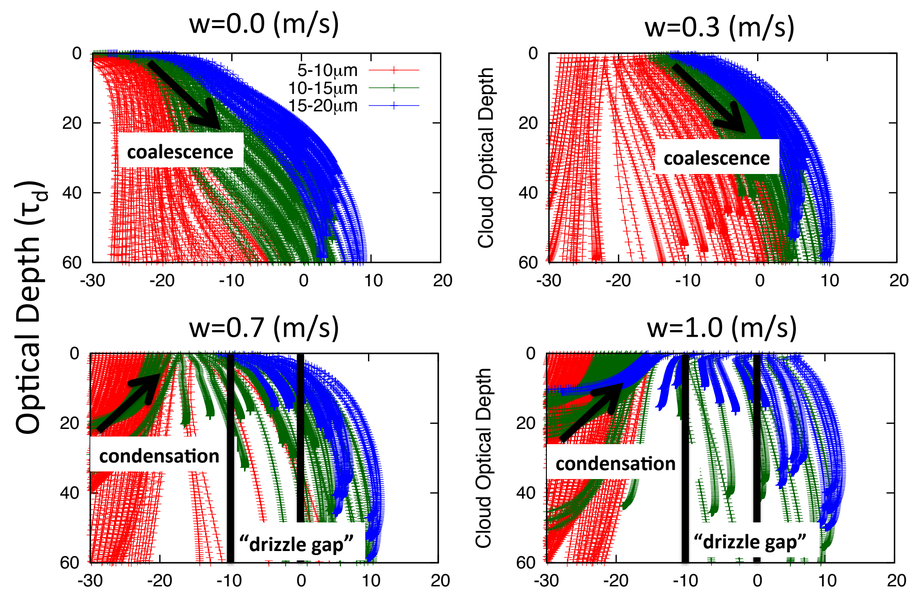

Re = 5-10μm
Re = 10-15μm
Re = 15-20μm

❖ **It shows clear "drizzle gap" when updraft becomes stronger.**

❖ **Coalescence process starts faster when updraft is weaker.**

7. Conclusions and Future Work

Although the intensities of convective updrafts in warm clouds have been paid less attention, **intensities of convective updrafts play a critical role in the warm rain formation process.** This study overcomes some of the challenges in observing microphysical processes in real clouds. **In the near future, we will extend our study to the cold rain formation process in deep convective clouds.**

Nakajima, T. Y., K. Suzuki., and G. L. Stephens (2010), Droplet growth in warm water clouds observed by the A-Train. Part II: A multi-sensor view. J. Atmos. Sci., 67, 1897–1907.

Suzuki, K., T. Y. Nakajima, and G. L. Stephens (2010), Particle growth and drop collection efficiency of warm clouds as inferred from joint CloudSat and MODIS observations. J. Atmos. Sci., 67, 3019–3032.

National Aeronautics and Space Administration

Jet Propulsion Laboratory
California Institute of Technology
Pasadena, California

www.nasa.gov

Acknowledgements

I am very thankful to have supportive co-workers. This research is supported by NASA grant NNN13D455T.
The CloudSat data products were provided by CloudSat Data Processing Center at CIRA/Colorado State University.

Poster No. EB-3

National Aeronautics and Space Administration

Multi-Model Evaluation of Cloud Phase Transition Using Satellite and Reanalysis Data

Principal Investigator: Gregory Cesana (329F)

Co-Investigators: D. E. Waliser (8000), X. Jiang (329F), F. J-L. Li (329F)

Objectives

Radiative effects of clouds are function of their micro- and macro-physical properties, which includes the cloud phase. Although the cloud phase is easy to determine for cloud colder than -40ºC (ice) and warmer than 0ºC (liquid), the processes happening in between are not well understood and documented. To reduce the uncertainties related to clouds in the context of climate change, the cloud phase representation in GCMs has to be constrained and evaluated with global scale observations.

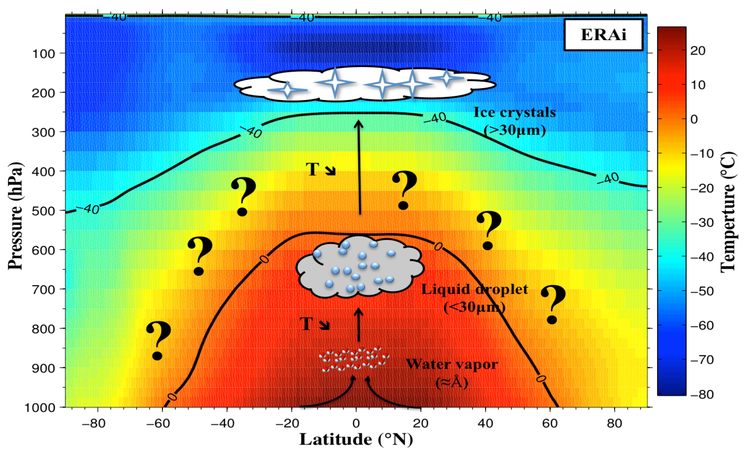

➔ **Develop a method to compare Obs and Models**

➔ **Characterize the cloud phase representation in the Models**

➔ **Evaluate T-dependent vs. complex microphysics schemes for cloud phase representation**

Tools

➔ **16 Models:**

- daily files, 2.5x2.5xL22 for 1 year of simulation
- 10 models from the GASS-YOTC Multi-Model Experiment database (7 prescribed SST & 3 coupled)
- 6 Models from the CMIP5/AMIP experiment (prescribed SST)

➔ **CALIPSO satellite:**

- High vertical resolution
- **Cloud phase retrieval independent of the temperature**
- Available over continents and reflective surfaces

Method

Definition of Phase Ratio (PR):

Model	**MPR = IWC / IWC+LWC**
Obs or Model+Sim	**FPR = Ice / Ice+Liq Cloud Frequency**

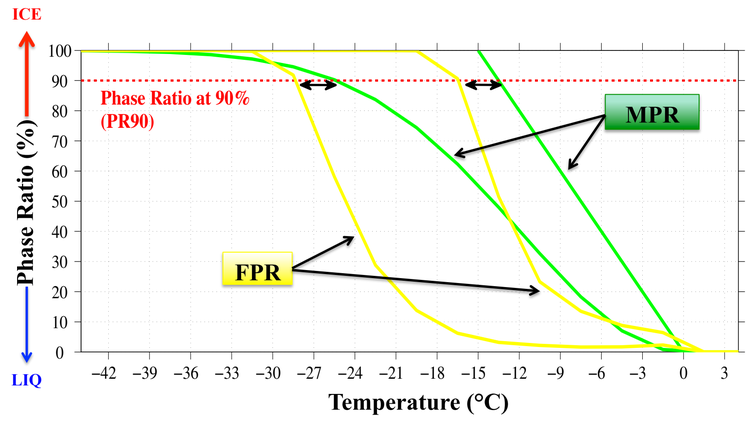

- Differences between the MPR and the FPR are reduced at 90% (PR90).
- There are less attenuation and noise in the Obs at PR=90%.
- Similar spatial-temporal grids are used to compare GCMs and Obs.

Zonal Cloud Phase

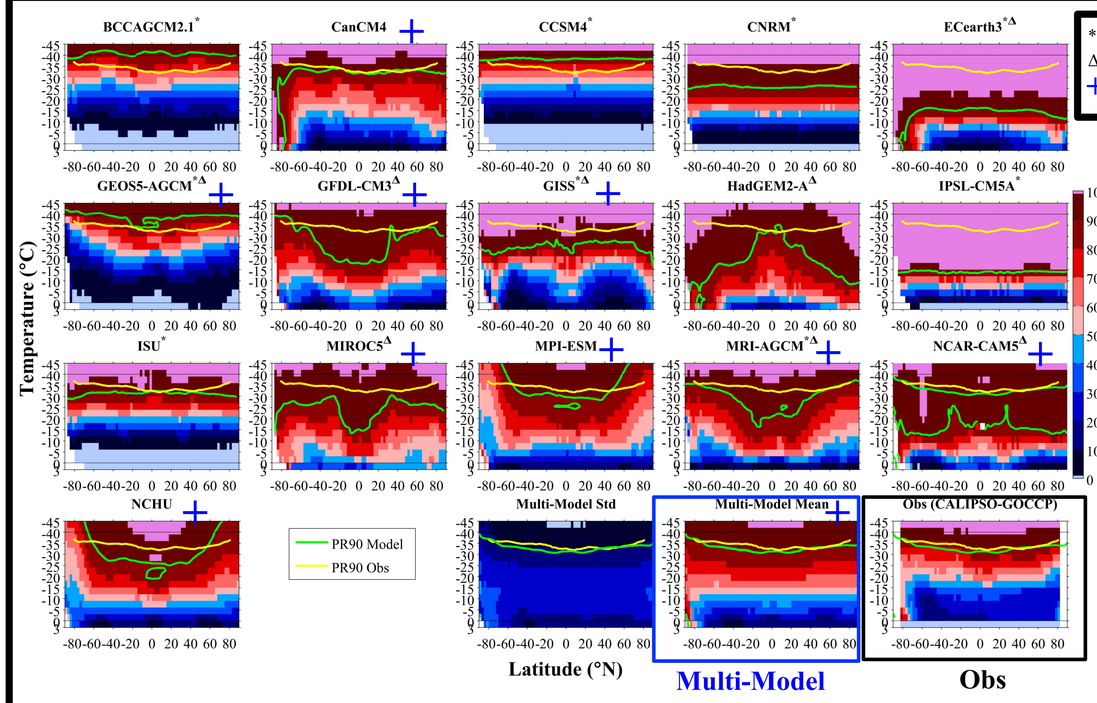

- 12/16 models exhibit a strong latitudinal dependence.
- The cloud phase transition temperature at 90% (**green line**, PR90) is highly variable depending on the model.
- Some models including T-dependent are able to reproduce the observed transition pretty well (yellow line).

➔ The multi-model mean cloud phase transition is in the range of uncertainty: -32.2°C vs. -33.7°C.

How to Easily Compare All Cloud Phase Schemes

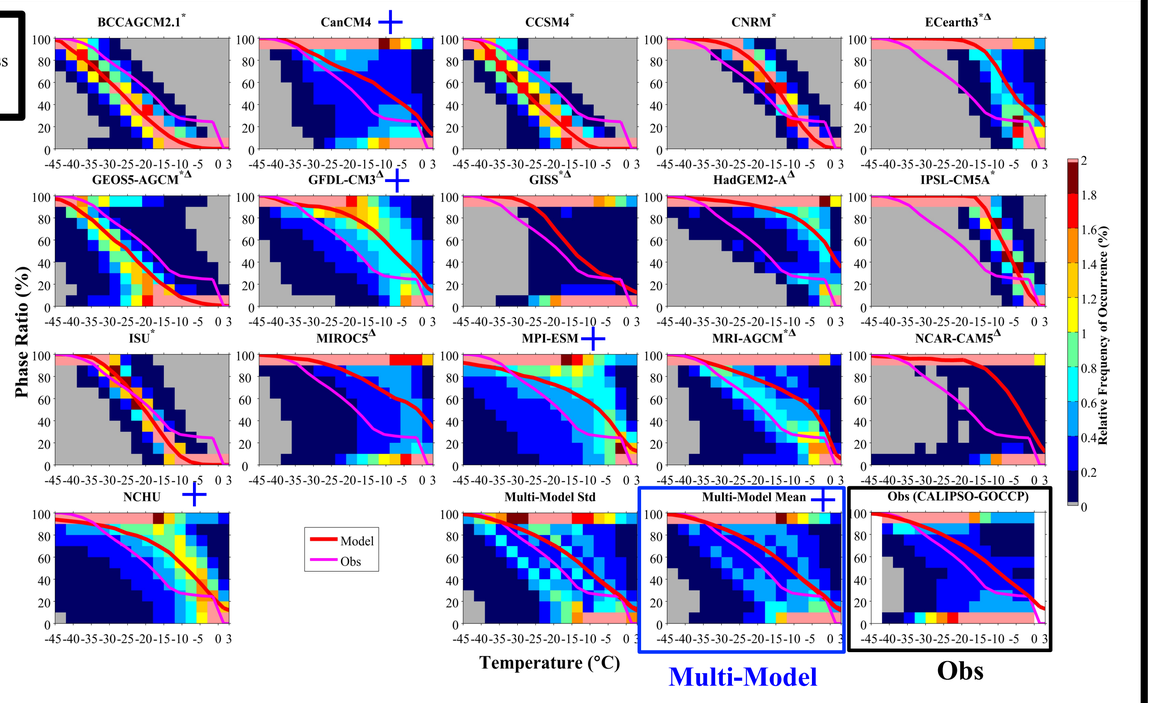

- This plot allows gathering large-scale processes and illustrating effects from convective processes.
- The observation biases inherent to the lidar sharpen the mean relation (magenta line):
  - overestimation of the ice-only and liquid-only cloud occurrences.
  - a cold bias.
- Some T-dependent models (CCS4, CNRM-CM5, ISU) produce too many mixed-phase clouds within too narrow temperature variability.
- The "biases-corrected" (warmer with less ice-only and liquid-only clouds) phase-temperature relation would be likely close to the multi-model mean and CanCM4, GFDL-CM3, MPI-ESM, and NHCU non T-dependent models.

Global Mean Temperature at PR90

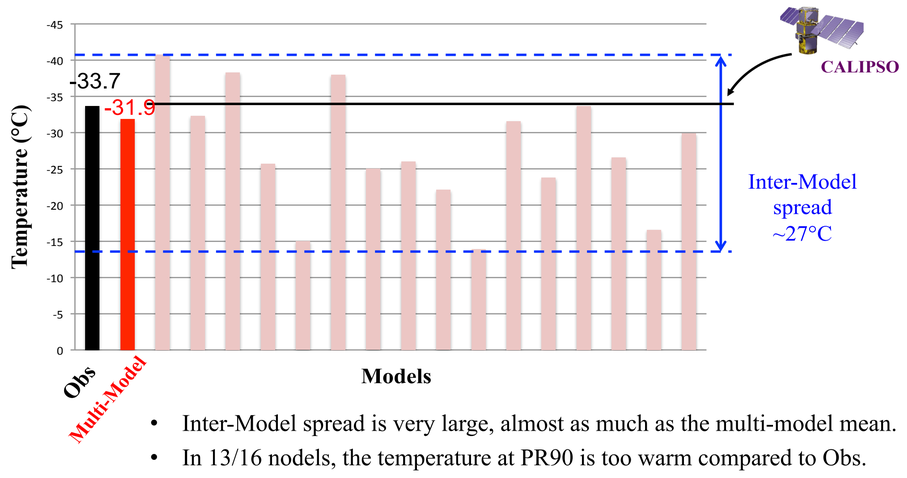

- Inter-Model spread is very large, almost as much as the multi-model mean.
- In 13/16 nodels, the temperature at PR90 is too warm compared to Obs.

Summary

Analysis of simulations from 16 GCMs and CALIPSO-GOCCP observations shows that some models can reproduce the relation between cloud phase transition and other variables (height, temperature, humidity, vertical velocity, precipitation, water vapor pressure), but none of them is able to perform well for all of these parameters:

- Only few models replicate the observed zonal variation of the Phase Ratio at 90% (PR90) as a function of the temperature.
- Apart from observations, models demonstrate a wide variation in Mass Phase Ratio across all latitudes/temperatures.
- For 13/16 GCMs, the cloud phase transition at PR90 is too low (6km to 8.4km) and temperature too warm (-13.9°C to -32.5°C) compared to observations (8.6km, -33.7°C).

Nevertheless, we highlighted that the best models were those that include complex microphysics and/or BF mechanism.

National Aeronautics and Space Administration

Jet Propulsion Laboratory
California Institute of Technology
Pasadena, California

www.nasa.gov

Reference:
Cesana, G., D. E. Waliser, X. Jiang, and J.-L. F. Li (2015), Multi-model evaluation of cloud phase transition using satellite and reanalysis data, J. Geophys. Res. Atmos., 120, doi:10.1002/2014JD022932.

Acknowledgements:
This research was carried out at the Jet Propulsion Laboratory, California Institute of Technology, under a contract with the National Aeronautics and Space Administration.

Poster No.: EB-4

National Aeronautics and Space Administration

Triple-frequency spaceborne cloud-precipitation radar simulation using a high-resolution atmospheric model

Principal Investigator: Jussi Leinonen (329F)

M. D. Lebsock (329F), S. Tanelli (334G), K. Suzuki (329F), H. Yashiro[1], Y. Miyamoto[1]

[1]RIKEN Advanced Institute for Computational Sciences, Kobe, Japan

Motivation

A successor for the current CloudSat and GPM spaceborne radar satellites was recommended by the 2007 decadal survey. The concepts for the next-generation mission (ACE, CaPPM) feature multi-frequency radars, which can greatly improve detection rate and retrieval accuracy, but their expected capabilities have not yet been quantified globally.

Research objectives

- Simulate the observations of a next-generation spaceborne triple-frequency cloud-precipitation radar
- Evaluate the expected performance globally at two orbital configurations (450 and 817 km altitudes)

Conclusions

The proposed system would have very good global coverage and significant improvements over the current missions. The detection rate at the 817 km orbit would be only marginally worse compared to the 450 km case, although multi-frequency retrieval capability would degrade somewhat.

Data

The Earth's atmosphere was simulated using NICAM (Nonhydrostatic Icosahedral Atmospheric Model):

- Global grid
- 875 m horizontal resolution

Methods

A radar model was built to simulate the observations:

- Melting layer reconstructed from rain, snow and graupel
- Single scattering modeled separately from cloud water, cloud ice, rain, snow, graupel and melting layer
- Multiple scattering simulated using a single-column time-dependent two-stream (TDTS) model

Results

The background map and the bar plots show the simulated availability of data at two different orbits. The availability is *color coded*:

- All bands
- W band only
- Ku and W bands
- Ka band only
- Ka and W bands
- Ku band only
- Ku and Ka bands
- Advanced processing required

A band is considered available if it is above the minimum detectable signal and not significantly affected by *attenuation*, *multiple scattering* or *nonuniform beam filling*.

- 450 km orbit — Better sensitivity, smaller footprint
- 817 km orbit — Better constellation opportunities

Results

The overview of global availability is shown below:

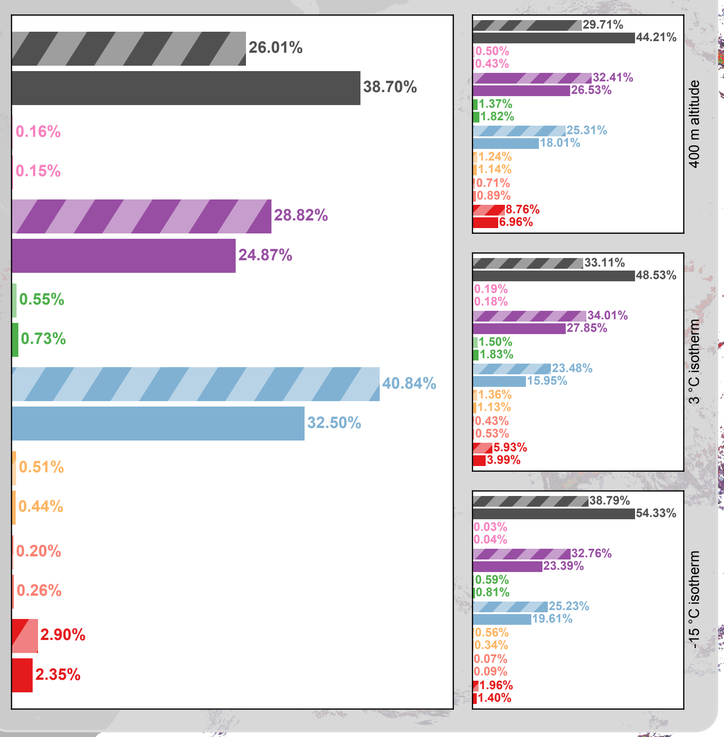

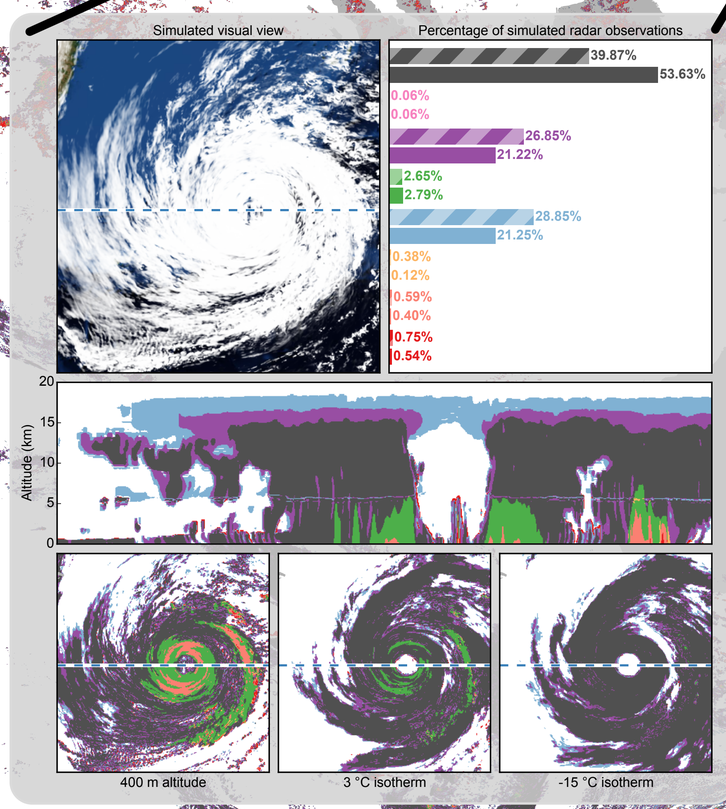

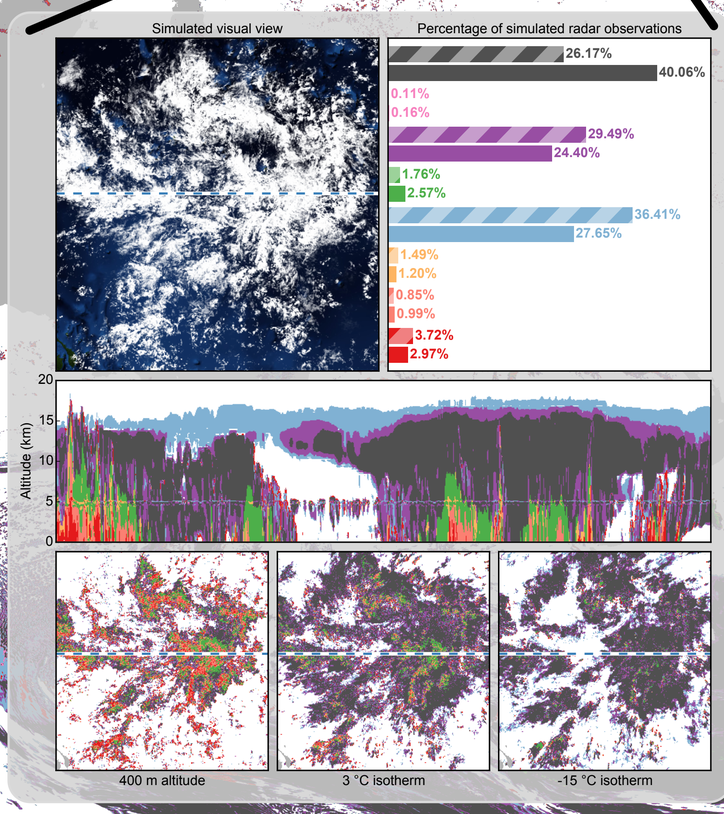

Simulated mission configurations

	450 km orbit		817 km orbit	
	Minimum detectable signal	Footprint size	Minimum detectable signal	Footprint size
Ku band (13.6 GHz)	0 dBZ	4.0 km	5 dBZ	7.3 km
Ka band (35.6 GHz)	-12 dBZ	1.4 km	-7 dBZ	2.5 km
W band (94.0 GHz)	-35 dBZ	0.85 km	-30 dBZ	1.2 km

For more information, see:
Leinonen et al., *Atmos. Meas. Tech. Discuss.*, 8, 4137–4189, 2015.

National Aeronautics and Space Administration

Jet Propulsion Laboratory
California Institute of Technology
Pasadena, California

www.nasa.gov

Poster No. EB-5

National Aeronautics and Space Administration

Spatio-temporal variations in onroad vehicle fossil fuel CO_2 emissions in Los Angeles Megacity

Principal Investigator: Preeti Rao (3290-Caltech)
[1]Kevin Gurney, Annmarie Eldering (3290), [1]Risa Patarasuk, [1]Yang Song, [1]Darragh O'Keeffe, Charles Miller (3290), Riley Duren (8000)
[1]School of Life Sciences, Arizona State University

1. INTRODUCTION:

❖Characterizing the spatio-temporal distribution of fossil fuel CO_2 ($FFCO_2$) emissions in urban landscapes is challenging.

❖We characterize onroad $FFCO_2$ emissions in the Los Angeles (LA) megacity using Hestia, an innovative bottom-up fine-resolution approach

❖LA megacity, comprising 153 cities and ~42% of California's population, contributes to ~43% of the state's $FFCO_2$ emissions.

❖Hestia-LA provides critical a priori estimates for atmospheric modeling, for validation of atmospheric CO_2 measurements by OCO-2 and other remote sensors

❖Unique dataset for carbon science, emissions mitigation & monitoring.

Road Class	Total road length (km)	FFCO2 emissions (tC/yr)	Emissions per road length (tC/km/yr)
Interstate	7,183	7,616,923 (40%)	1,060
Arterial	13,122	7,890,541 (41%)	601
Collector	4,997	1,445,517 (8%)	289
Local	NA	2,049,819 (11%)	NA
Total		**19,002,800 (100%)**	

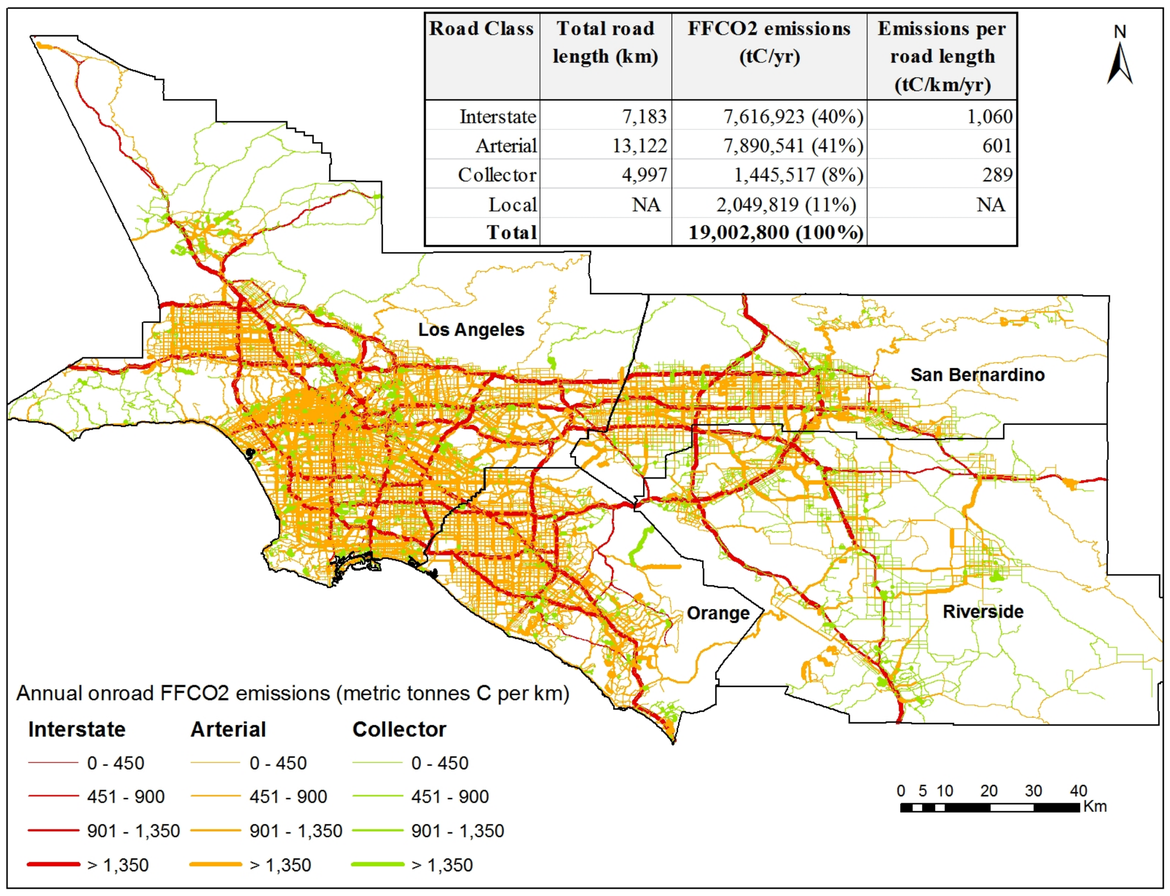

2. OBJECTIVES:

- ❖ Develop onroad $FFCO_2$ emissions data product at the spatial scale of buildings and streets at hourly time steps for the LA megacity.
- ❖ Analyze emission patterns across time and space esp. emissions hotspots.
- ❖ Demonstrate its significance in developing mitigation policies at the scale of cities and neighborhoods

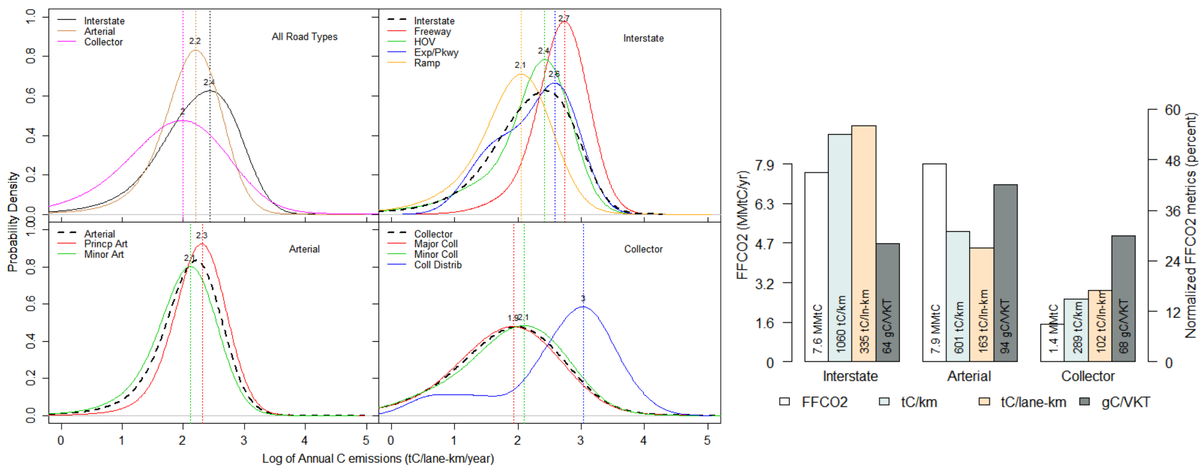

4. SIGNIFICANCE and CONCLUSION

❖Onroad $FFCO_2$ emissions are 49% of the total megacity emissions.

❖Identified C emission hotspots and characterized the variability in onroad C emissions at fine spatial (250m) and temporal (hourly) scales.

❖Hestia-LA provides critical a priori estimates of FFCO2 emissions for use in high-resolution atmospheric modeling of CO2 and helps validate other atmospheric observations of CO2.

❖Onroad FFCO2 emissions data product– relevant for improving local and state-level inventories, supporting mitigation policy evaluation and planning by local decision makers.

3. METHODS:

Annual traffic volume – SCAG
Temporal traffic info. – PeMS CALTRANS
Annual CO_2 emissions – CARB's EMFAC model

↓

Allocate annual $FFCO_2$ to road segments based on vehicle km traveled & road type

↓

Spatio-temporal structure of onroad emissions

Other analyses included:
- ❖ Explore emissions metrics
- ❖ Geo-spatial analysis of hotspots
- ❖ Statistical & uncertainty analysis

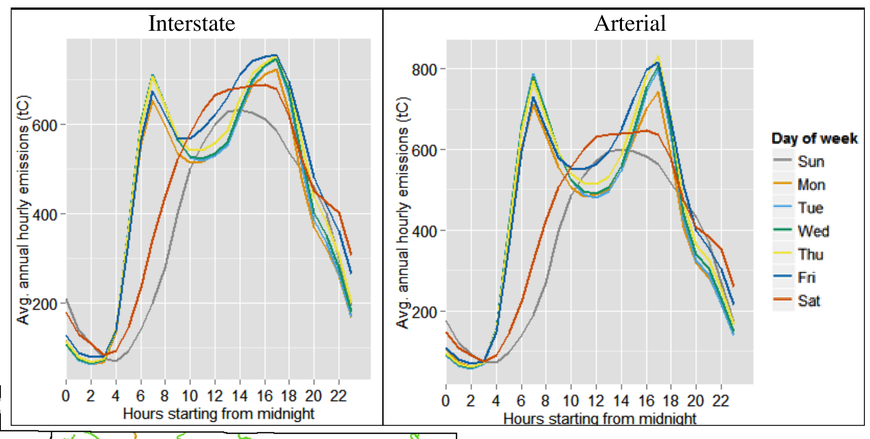

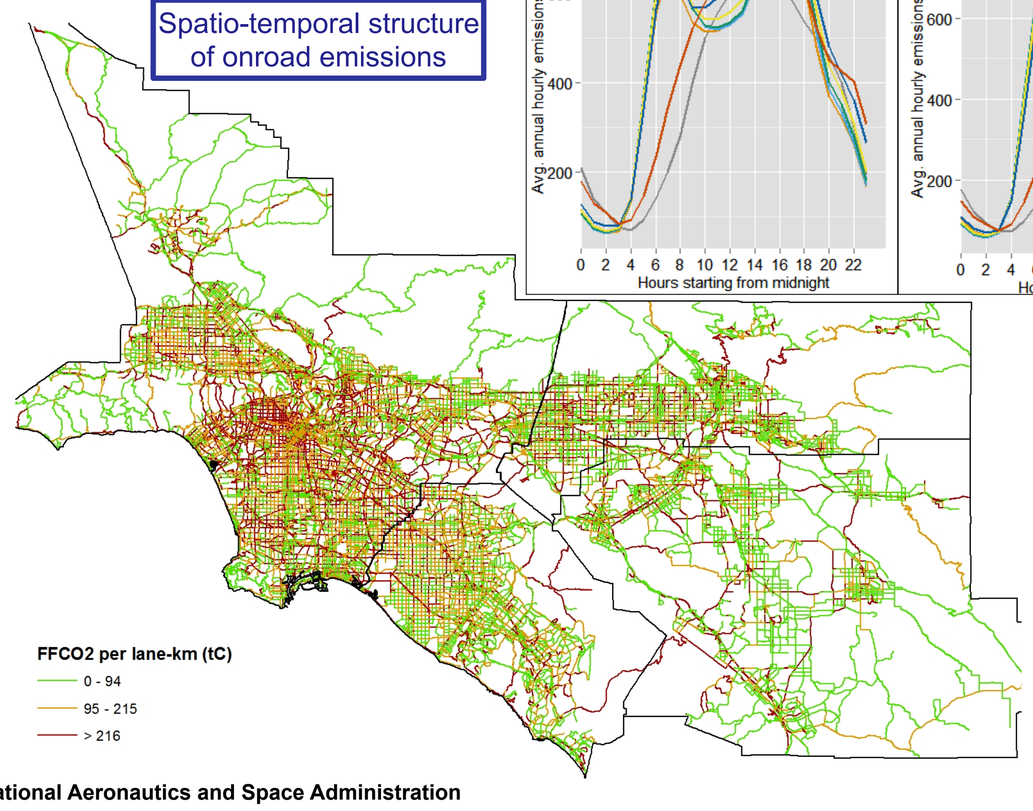

Road Class	Road length (ln-km)	VKT (billion km)	$FFCO_2$ (10^3 tC)	tC/ln-km	gC/VKT
ALL ROAD TYPES (Top 5%)					
Interstate	4,212 (86%)	49 (76%)	3,130 (76.5%)	743	64
Arterial	281 (6%)	4 (6.5%)	389 (9.5%)	1,387	95
Collector	424 (8%)	11 (17.5%)	574 (14%)	1,354	52
TOTAL	**4,917 (100%)**	**63.87 (100%)**	**4,094 (100%)**		
ROAD TYPES OTHER THAN INTERSTATES (Top 5%)					
Arterial	1,087 (61%)	8 (40%)	779 (52%)	717	96
Collector	708 (39%)	12 (60%)	721 (48%)	1,019	60
TOTAL	**1,794 (100%)**	**20 (100%)**	**1,500 (100%)**		

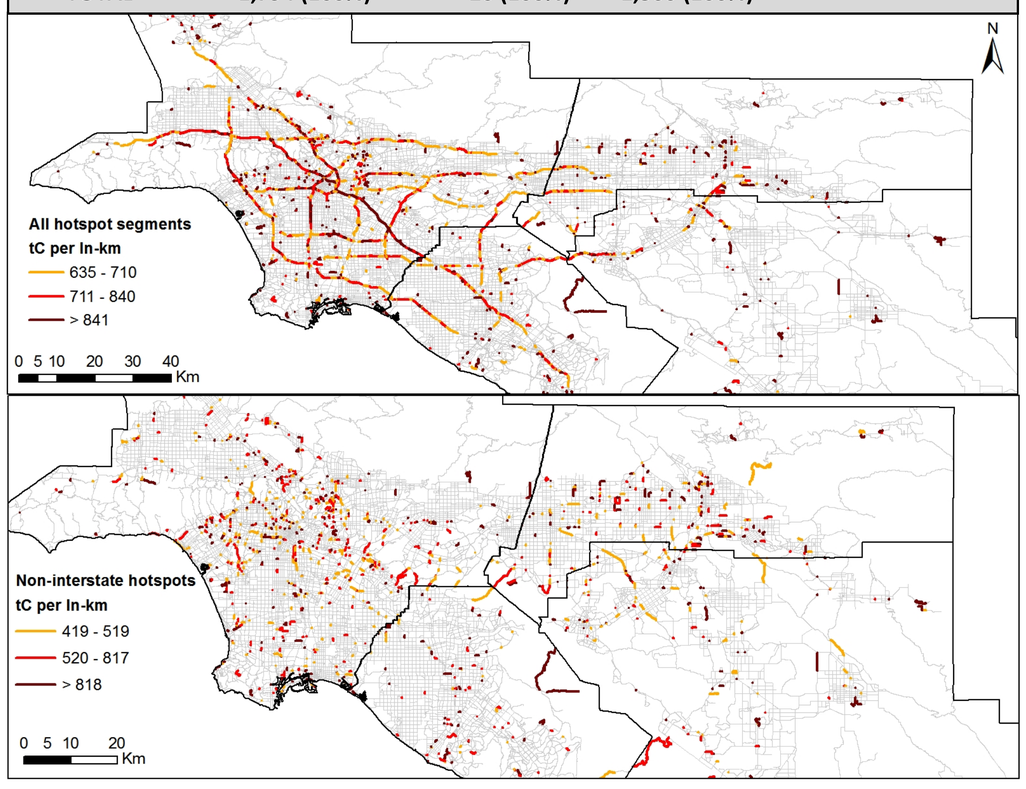

National Aeronautics and Space Administration
Jet Propulsion Laboratory
California Institute of Technology
Pasadena, California

www.nasa.gov

Acknowledgements: This research is supported by the National Institute of Standards and Technology (NIST) Greenhouse Gas Measurement Science Program through interagency agreement with NASA

Poster No. EB-6

National Aeronautics and Space Administration

Evaluation of CO Distribution and Variation in the UTLS from GMI and GEOS-Chem Simulations by Using Aura MLS Observations

Principal Investigator: Lei Huang[1] (329K)

Jonathan H. Jiang[1] (329K), Lee Murray[2], Megan Damon[3], Hui Su[1] (329K)

1. Introduction

Carbon monoxide (CO) :

•Produced by incomplete combustion of carbon-based fuels and oxidation of methane and non-methane hydrocarbons

•Play an important role in global atmospheric chemistry and radiation balance

•Lifetime of 1–2 months in the tropical troposphere, a useful tracer for studying the mass transport of polluted air

•Large seasonal and interannual variability in the troposphere, affected by many factors (emission, photochemistry, transport).

Motivation:

(1) How model performs in the UTLS region is still not clear.

(2) New version (V4.2) of MLS CO data eliminates the biases in previous versions and thus more accurate

Objectives of this study:

- Evaluate CO simulations in the UTLS from two CTMs: GMI and GEOS-Chem.
- Investigate relationships between surface emission, convection and UT CO in model simulations.

2. Observation & Model Data

Satellite Data:

Aura MLS Level 2 data (V3.30, V4.20)

Model Data:

GMI and GEOS-Chem simulations

•Time period: 2004–2012

•Driven by MERRA meteorology

•FF, BF, BB emission varies yearly

•BB emission from GFED3 data

•GMI: 72 levels, all fixed

•GEOS-Chem: 47 levels, fixed above 177 hPa

•Temporal resolution: monthly

•Spatial resolution: 2° × 2.5°

3. Seasonal Distributions of CO in the UTLS

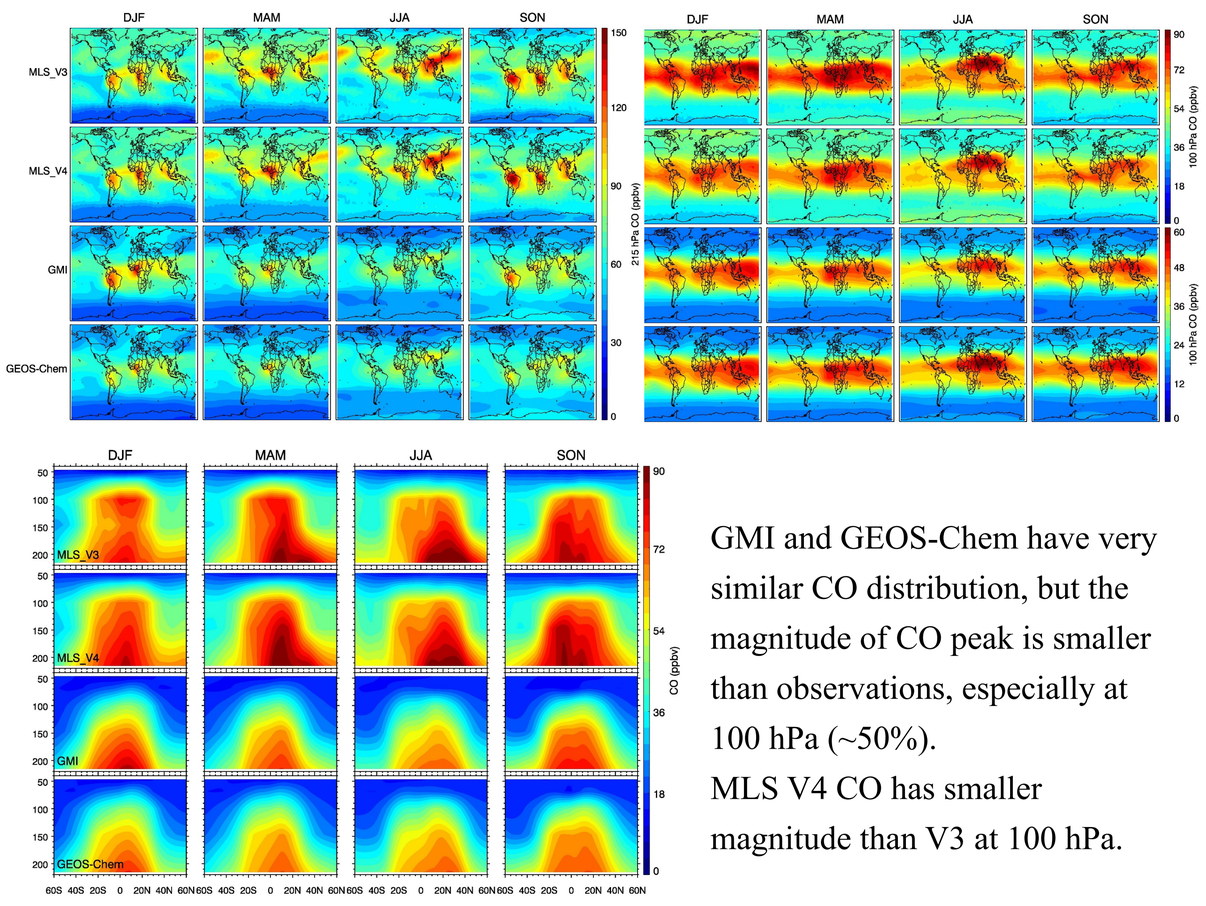

GMI and GEOS-Chem have very similar CO distribution, but the magnitude of CO peak is smaller than observations, especially at 100 hPa (~50%).

MLS V4 CO has smaller magnitude than V3 at 100 hPa.

4. Monthly Variations of CO in the UTLS

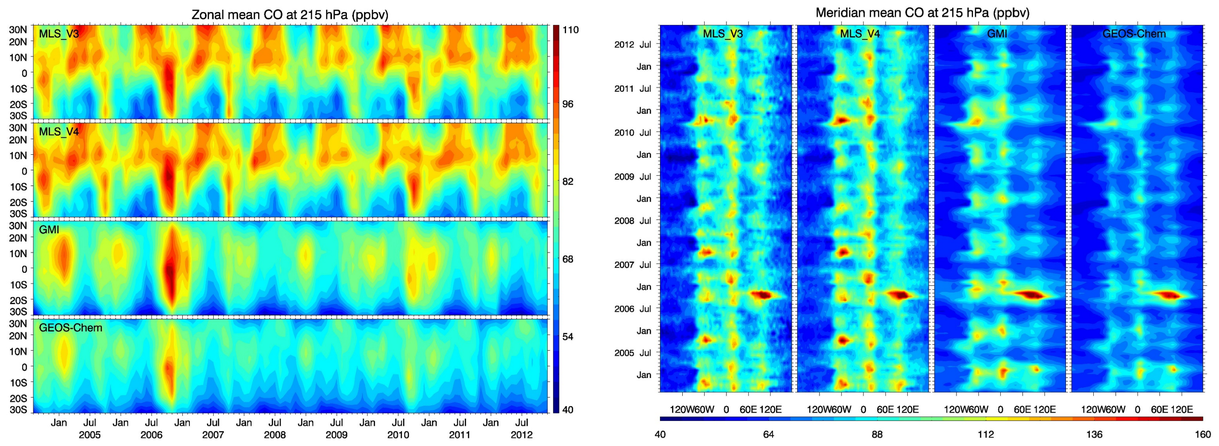

5. Regional Analysis

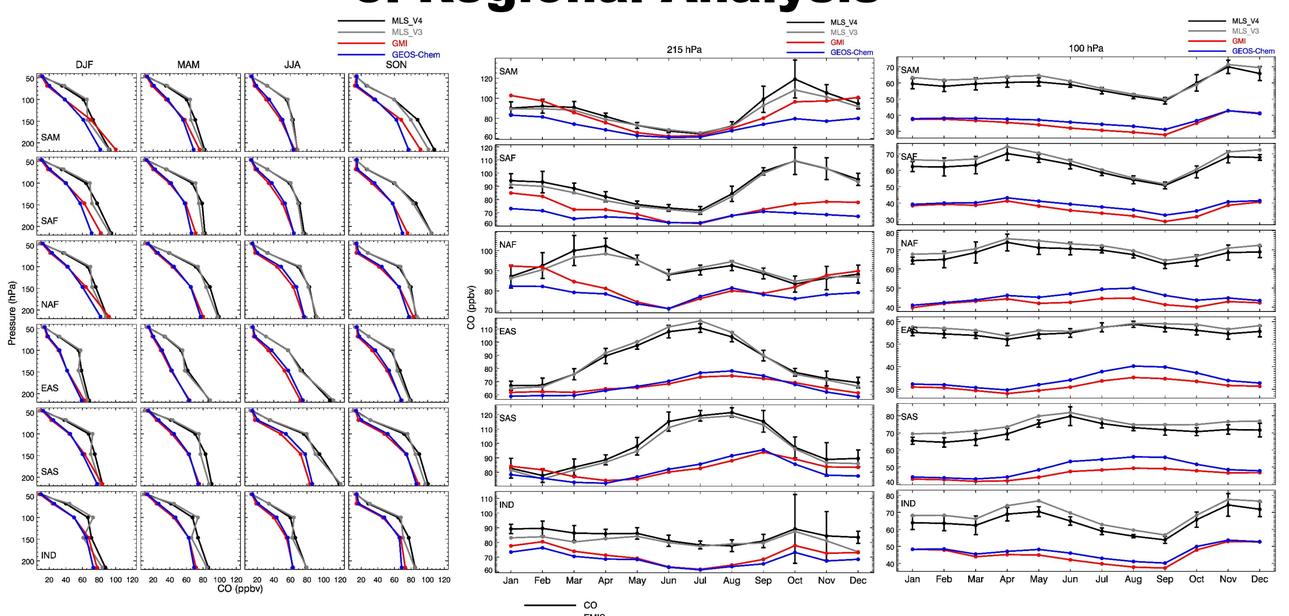

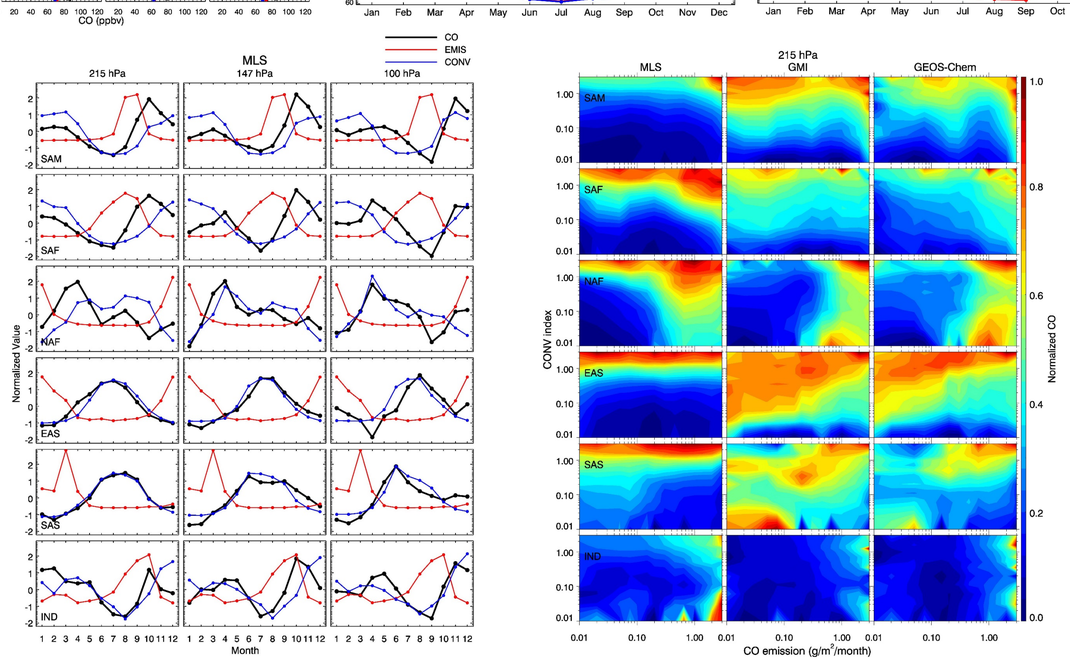

6. Conclusions

- GMI and GEOS-Chem simulations of CO are similar in spatial distribution and magnitude. The seasonal distributions of CO simulated by models are in better agreement with MLS in the SH than in the NH.
- The CO tape recorder simulated by models has better agreement with MLS in the tropics and SH subtropics than NH subtropics.
- The seasonal cycle of CO in the UTLS are not well simulated over most regions where high CO centers are located above.
- Different emission-convection-CO relationships are shown over different regions. Such relationships in the two models' simulations are consistent with these in MLS observations over some regions at 215 hPa and 147 hPa.

Poster No. EB-7

National Aeronautics and Space Administration

Jet Propulsion Laboratory
California Institute of Technology
Pasadena, California
www.nasa.gov

[1]Jet Propulsion Laboratory, California Institute of Technology, Pasadena, CA

[2]NASA Goddard Institute for Space Studies, New York, NY

[3]NASA Goddard Space Flight Center, Greenbelt, MD

National Aeronautics and Space Administration

Characterization of methane super-emitters

Principal Investigator: Francesca Hopkins (329L)
Riley Duren (8000), Charles Miller (3290), Andrew Aubrey (382D), Simon Hook (3290),
Glynn Hulley (329B), Bill Johnson (389N), Le Kuai (329L), Andrew Thorpe (382D), John Worden (3290)

Motivation

- Methane (CH_4) is a powerful greenhouse gas and atmospheric pollutant
- CH_4 mitigation is needed to comply with California's Global Warming Solutions Act (2006 Assembly Bill 32)
- A preponderance of CH_4 sources and poor air quality in California's southern San Joaquin Valley make it an optimal target for CH_4 mitigation
- However, fundamental information about CH_4 emissions is necessary:
  - **What are the largest sources of methane?**
  - **Where are these sources located?**
  - **How much can CH_4 be reduced by curtailing large emitters?**

Elevated CH_4 in the San Joaquin Valley

Observed from satellite (Kort et al. 2014):
SCIAMACHY 2003-2009 avg. CH_4 anomaly (ppb)

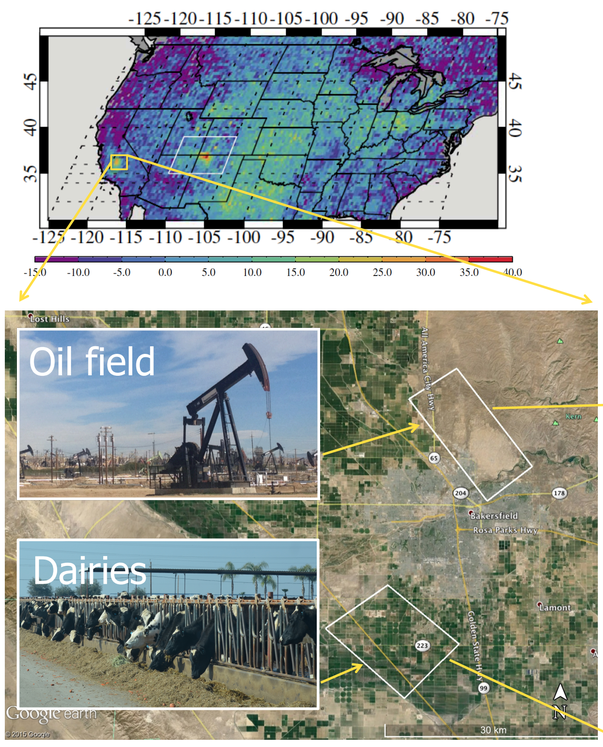

Super-emitters sources detected by HyTES
Super-emitters in each source category as a fraction of total number of possible sources

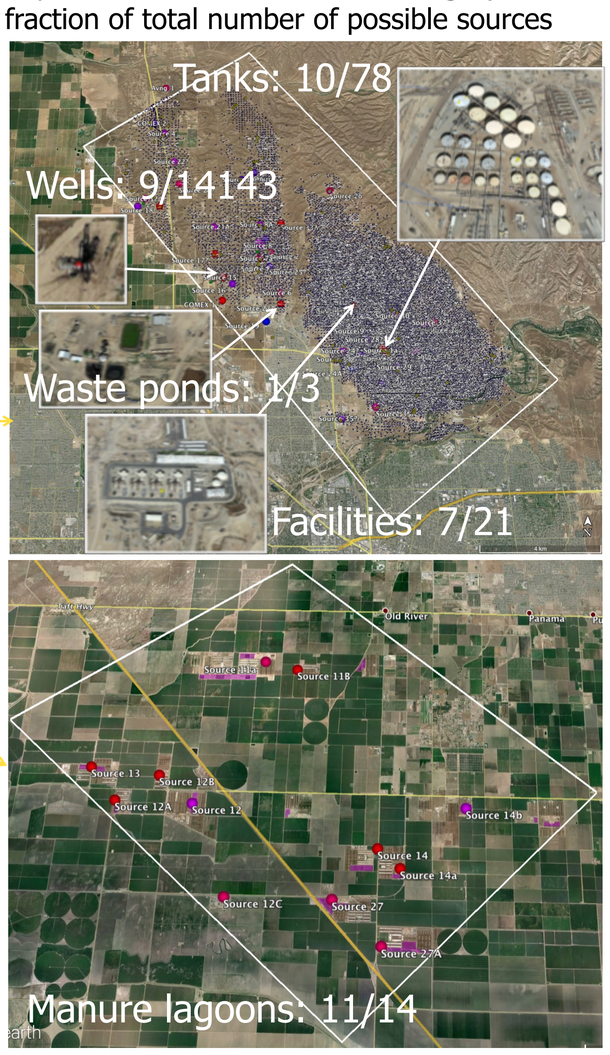

Study areas: Oil field with highly concentrated oil extraction infrastructure (upper panel) and area with many large dairies (lower panel) were repeatedly sampled by JPL airborne platforms and complementary ground measurements in 2014 and 2015

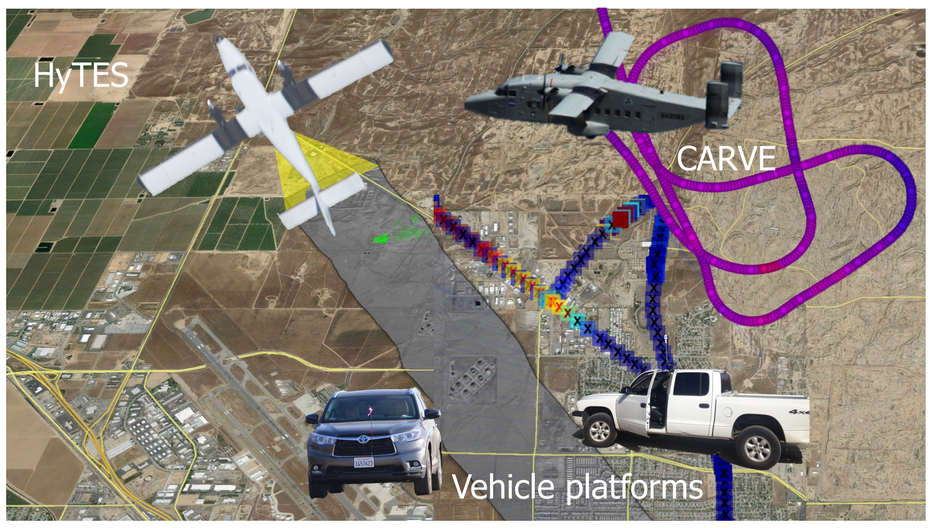

Tiered observation approach

- **Satellite** imagery defines regions with elevated column CH_4
- JPL's **Hyperspectral Thermal Emission Spectrometer** (HyTES) images suspected CH_4 source areas from aboard an aircraft
- **Clutter matched filter retrievals** (CMF) of **HyTES** data identify CH_4 "super emitters" with criteria of repeated plume observations
- **Controlled release of CH_4** determines lower limit of **HyTES** detection: minimum threshold for "super-emitters"
- **Airborne and on-road observations** of in situ CH_4 mole fraction: verify CH_4 plumes, provide a data constraint for CH_4 flux estimation
- **Long-wave infrared camera**: ground observation of super-emitters pinpoints CH_4 emission source, temporal emission patterns

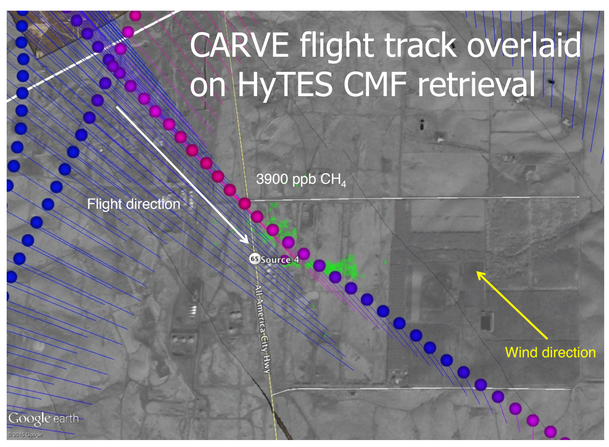

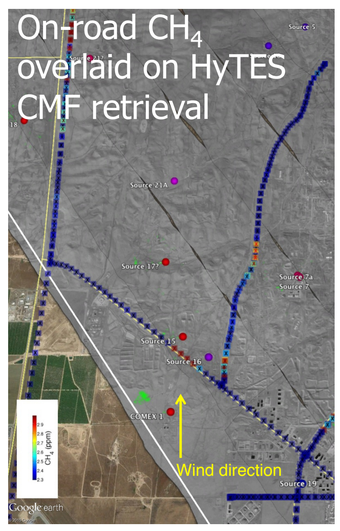

CH_4 mole fractions measured aloft with the CARVE aircraft (*left*) **and on-road** (*right*) **in the Kern River oil field confirm CH_4 enhancements detect by HyTES CMF retrievals** *(green plumes)*

Super-emitter contribution to CH_4 emissions

- Using a conservative lower limit for HyTES detection from a controlled release experiment, we estimated a minimum CH_4 flux for super-emitters
- We determined the relative contribution of super-emitters by dividing minimum flux by estimated inventory CH_4 for the same area

Repeated plume observations with HyTES CMF retrieval → Controlled release detection limit: 500 SCFH = 85 tons CH_4 y^{-1} → California 0.1° CH_4 inventory (Jeong et al. 2012; 2014)

Study area	Number of super-emitters	Minimum CH_4 from super-emitters	CALGEM CH_4 inventory emissions	Percent of total CH_4 emissions from super-emitters
Oil field	28	2.4 kton CH_4 y^{-1}	8.3 kton CH_4 y^{-1}	≥ 29%
Dairies	12	1.0 kton CH_4 y^{-1}	4.8 kton CH_4 y^{-1}	≥ 21%

Conclusions and Future Work

- ***HyTES detected multiple types of super-emitters in the oil field, but only one type– manure lagoons– among dairies***
- ***Super-emitters are distributed differently across source types***
  - Oil processing and storage facilities were much more likely to be super-emitters than oil wells or gas pipelines
  - Most manure lagoons were super-emitters
- ***Super-emitters constitute a large proportion of CH_4 emissions***
  - Reducing CH_4 from super-emitters will likely be an effective mitigation strategy
  - Quantitative retrievals of HyTES CH_4 will reveal relative strength of different plumes, hence better inform emission estimates
  - Forward atmospheric model simulations tuned with in situ CH_4 observations will enable better quantification

National Aeronautics and Space Administration
Jet Propulsion Laboratory
California Institute of Technology
Pasadena, California

www.nasa.gov

References

Kort, E.A., C. Frankenberg, K.R. Costigan, R. Lindenmaier, M.K. Dubey, D. Wunch (2014), Four corners: The largest US methane anomaly viewed from space, *Geophysical Research Letters, 41,* 6898-6903.

Jeong, S., C. Zhao, A.E. Andrews, L. Bianco, J.M. Wilczak, M.L. Fischer (2012), Seasonal variation of CH4 emissions from central California, *Journal of Geophysical Research, 117,* D11306.

Poster No. EB-8

Remote-sensing constraints on South America fire traits by Bayesian fusion of atmospheric and surface data

A. Anthony Bloom[1], John Worden[1], Zhe Jiang[1], Helen Worden[2], Thomas Kurosu[1], Christian Frankenberg[1], Felix Landerer[1], David Schimel[1]

[1]Jet Propulsion Laboratory/ California Institute of Technology, Pasadena, CA, U.S.A.
[2]National Center for Atmospheric Research, Boulder, CO, U.S.A.
*abloom@jpl.nasa.gov

2006-2011 South America fire CO and burned area

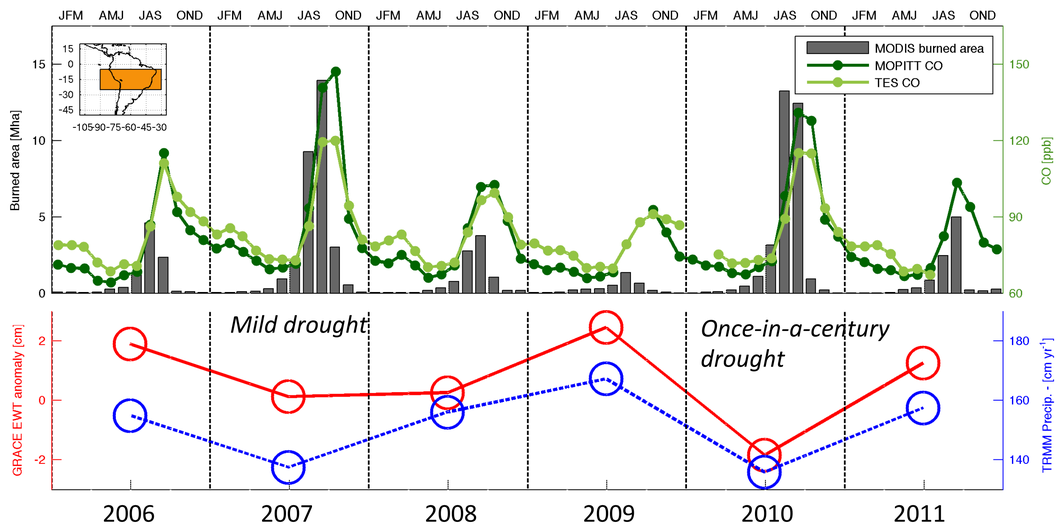

Figure 1: Monthly MODIS burned area, Aura TES CO and Terra MOPITT CO (top). Mean Annual GRACE equivalent water thickness and TRMM precipitation (bottom).
Bloom et al., 2015 *GRL*

Two major fire years: 2007 and 2010

- Larger burnt area (+5%) but lower CO emissions (-28%) in 2010 fires.
- A major drought occurred in 2010.
- How did fire traits and C losses differ between 2007 and 2010?

box 1

2007 and 2010 South America fires comparison

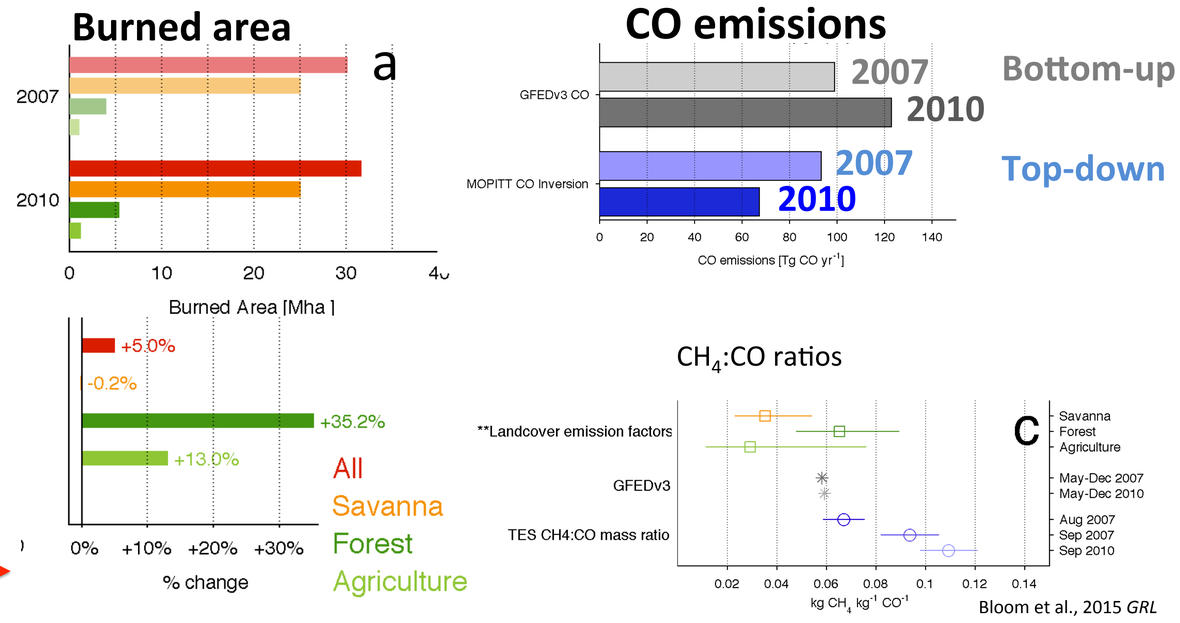

Bloom et al., 2015 *GRL*

Figure 2(a): 2007 and 2010 MODIS savanna, forest, agriculture and total burned area (GFEDv4; Giglio et al., 2010). (b) GFEDv3 C losses, CO and MOPITT CO inverse emission estimates (c) Andreae & Merlet (2001) CH_4:CO values, GFED v3 CH_4:CO and TES derived CH_4:CO (see box 5).

- Larger forest (+35%) and agriculture (+13%) burnt area, small difference in savanna & grassland burnt area (-0.2%)
- Increase in 2010 fire CH_4:CO ratio
- Bottom-up 2010 CO emissions are higher (+24%); Top-down CO emissions are lower (-28%).
- **Differences in biomass density, land-cover type, CH_4:CO emission ratios do not explain observed CH_4:CO, CO and burned area trends .**

box 2

2007-to-2010 changes in combusted biomass density & combustion efficiency.

$$F_{s,b} = A_b \, CBD_b EF_{s,b}$$

F = fire C fluxes
A = Burnt area
CBD = Combusted Biomass Density
EF =Emission factors
b =land-cover type (sav., for., agr.)
s =species (CO_2,CH_4,CO)

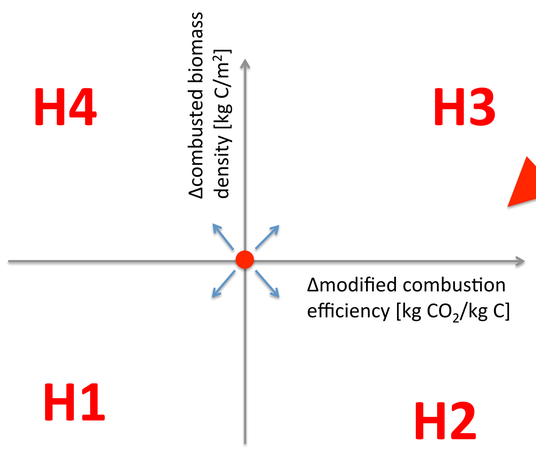

Figure 3: Hypotheses on the possible 2007-to-2010 changes (Δ) in combusted biomass density and combustion efficiency.

Table 1. Hypotheses 1–4[a]

Hypotheses	Change in 2010 Combusted Biomass Density (CBD) and Combustion Efficiency (MCE), Relative to 2007
H1	Decrease in CBD and decrease in MCE.
H2	Decrease in CBD and increase in MCE.
H3	Increase in CBD and increase in MCE.
H4	Increase in CBD and decrease in MCE.

[a]Hypotheses 1–4 outline all combinations of combusted biomass density (CBD: [combusted biomass]/[area]; unit in kg m^{-2}) and modified combustion efficiency (MCE: $[CO_2]/[CO_2 + CO + CH_4]$; unit in (kg C) (kg C)$^{-1}$) changes between 2007 and 2010.

box 3

Method: we perform a Bayesian inversion (using a Markov-Chain Monte Carlo algorithm) to determine the probability of 2007 and 2010 CBD and MCE values (see box 3), and total C losses. We use MODIS burnt area, a pan-tropical biomass map to determine total fluxes. We constrain fire C fluxes based on MOPITT CO, TES CH_4:CO and emission factors.

2007-to-2010 changes in South America fires traits: decrease in combusted biomass and increase in combustion efficiency is the most probable outcome.

1. **Relative to 2007 fires, we find:**
- 88% probability of lower 2010 combusted biomass density
- 72% probability of lower 2010 CO emissions
- 82.4% probability of lower C losses from 2010 fires

2. **Lower 2010 combustion completeness is consistent with:**
- 4-6% reduction in GOME-2 SIF[1] during the preceding wet season, and
- 0-8% reduction in biomass due to repeat fires.

3. **Additional constraints – OCO-2 and GEDI – are needed to resolve inter-annual variations on fire traits and emissions.**

TES South America CH_4:CO & dry season CH_4 peak

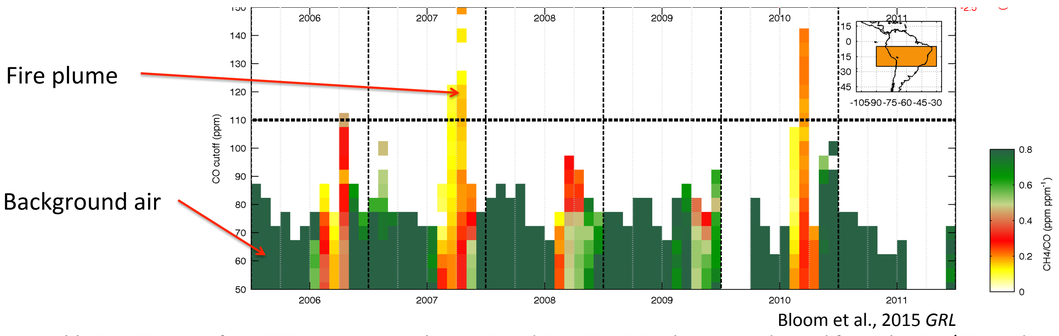

Bloom et al., 2015 *GRL*

Figure 5: monthly CH_4:CO ratios from TES mean tropospheric CO and CH_4; CH_4:CO values were derived from the CH_4/CO gradients for points where CO> CO cutoff (top).

- Fire plume CH_4:CO consistent with measured CH_4:CO (box 2)
- Increase in 2010 CH_4:CO consistent with increased contribution from forest fires.

box 4

Hypothesis tests

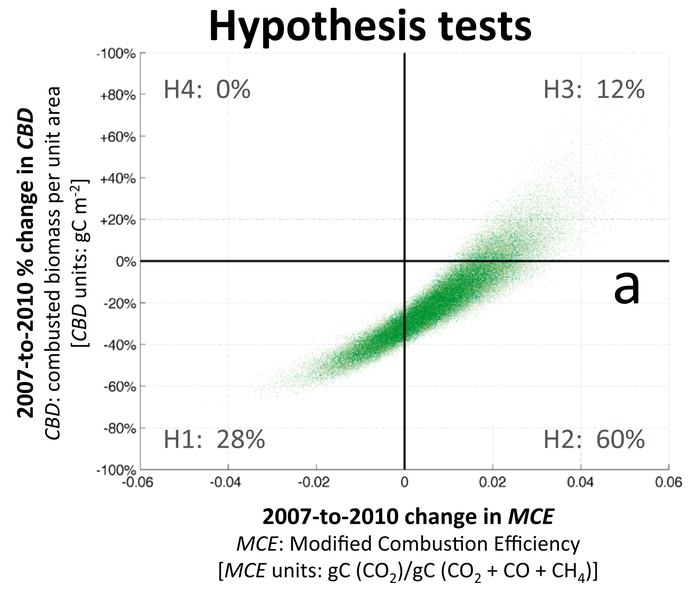

Total C emissions

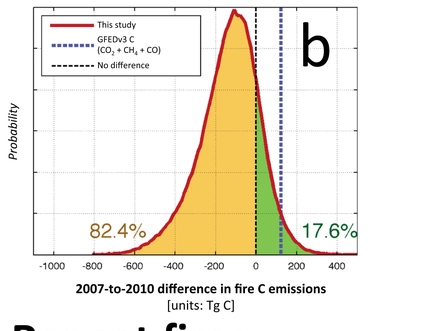

Repeat fires

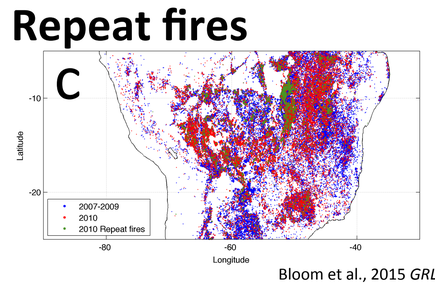

Bloom et al., 2015 *GRL*

Figure 4(a): Probability distribution of 2007-to-2010 normalized differences in overall combusted biomass density (CBD) and modified combustion efficiency (MCE); probability of hypotheses H1-H4 (see box 3) are shown within each quadrant (b) Probability distribution of 2007-to-2010 difference in total C loss (c). Location of 2007-2009 fires, 2010 fires, and repeat 2010 fires (i.e. 2010 & 2007-2009 co-located fires)

Bloom, A. Anthony, et al. "Remote sensing constraints on South America fire traits by Bayesian fusion of atmospheric and surface data." *Geophysical Research Letters* (2015).
Joiner, J., et al. "Global monitoring of terrestrial chlorophyll fluorescence from moderate-spectral-resolution near-infrared satellite measurements: methodology, simulations, and application to GOME-2." (2013).

box 5

Poster no. EB-9

National Aeronautics and Space Administration

Seasonal Transport of Asian Ozone and PAN Using Aura TES PAN Retrievals

Zhe Jiang
John Worden, Vivienne H. Payne, Liye Zhu, Emily Fischer, Thomas Walker, Dylan Jones

Introduction

As an important reservoir for reactive nitrogens (NO_x), peroxyacetyl nitrate (PAN) plays a significant role in global ozone (O_3) chemistry. However, little is known about the distribution and seasonality of PAN and its relative contribution on long-range O_3 transport. Here, we use six years of PAN observations in April and July from the Aura Tropospheric Emission Spectrometer (TES) to show that East Asian PAN export has a springtime maximum. Model sensitivity analysis indicates that the relative contribution of East Asian PAN to long-range O_3 transport is about 20% in spring, confirming the important role of PAN on global O_3 distribution. The relative contribution of East Asian PAN to long-range O_3 transport is much smaller in summer (about 10%). The pronounced seasonality of role of East Asian PAN is mainly driven by the strong springtime westerly wind over northwest Pacific, and the high summertime O_3 production efficiency over East Asia. Although emissions from East Asia are important sources for transpacific O_3 transport to western North America, our results reveals that boreal Asia fires have comparable contribution on the air quality over western North America. This study highlights the importance of accounting for the seasonality of PAN magnitude, local chemical environment and transport in evaluating how PAN affects global O_3 levels.

Model and observations

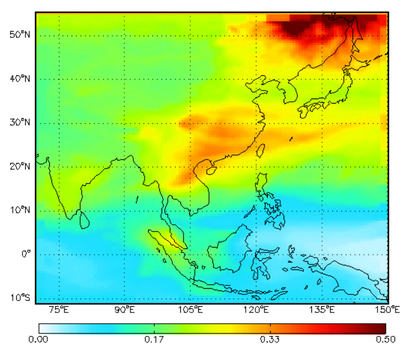

- Free tropospheric PAN mixing ratio in April 2008 (about 500 hPa) with unit ppb.
- We use version v9-01-01 of the GEOS-Chem model driven by GEOS-5 meteorological fields with detailed tropospheric O_3-NO_x-hydrocarbon chemistry.
- Updated PAN scheme as described in Fischer et al. [2014].

Tropospheric Emission Spectrometer (TES) PAN measurements

- Measurements of free tropospheric PAN from the Aura-TES satellite instrument, provided by Payne et al. [2014].
- TES can measure elevated PAN, with a detection limit of approximately 0.2 ppbv and uncertainties between 30% and 50%. The sensitivity of the TES PAN retrievals peaks in the free troposphere.

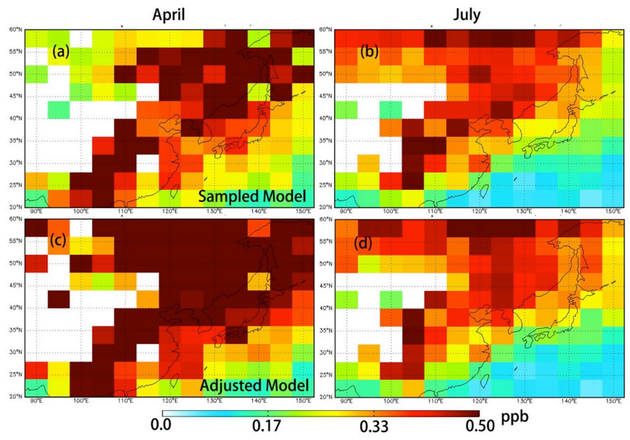

- Multi-year monthly mean value of free tropospheric PAN (800 - 400 hPa) in April and July 2005 - 2010. (a-b) GEOS-Chem simulation, sampled at TES measurment locations and times; (c-d) Adjusted model simulation using TES PAN measurements.
- Over the East China outflow region (20°-40°N), the strong westerly wind results in obvious springtime PAN export maximum, and the primary source is the anthropogenic emissions from China.

Transpacific transport of Asian O_3 and PAN

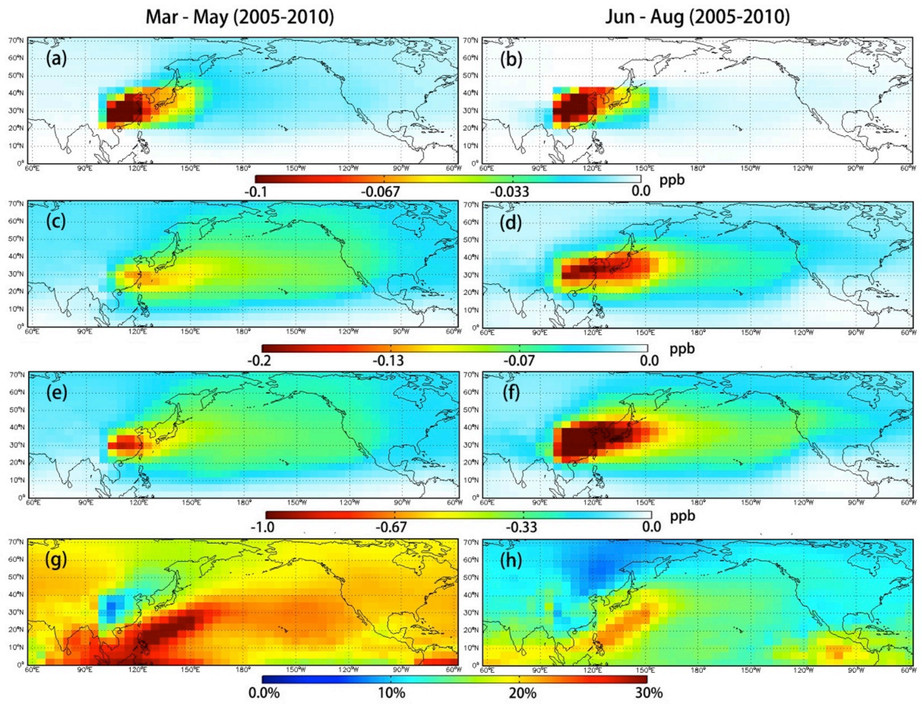

- Multi-year seasonal mean value of response of free trospheric O_3 and PAN (800 - 400 hPa) to East Asian (97.5-152.5°E, 20-44°N) NO_x and PAN perturbation.
- (a,b) Change of PAN due to no East Asian PAN formation. It represents East Asian PAN, which is about 0.15 ppb over East China in both seasons.
- The value is much higher in spring than that in summer over the middle and east Pacific, reflecting the effect of more PAN export due to strong westerly winds.
- (c,d): Change of O_3 due to 10% reduction of East Asian PAN formation. The larger influence over East Asia in summer is due to higher O_3 production efficiency. On the contrary, the influence over middle and east Pacific is larger in spring than that in summer due to more PAN export.
- (e,f): Change of O_3 due to 10% reduction of East Asian NO_x emission.
- (g,h): Relative contribution of PAN on free tropospheric O_3, calculated by Fig.(c,d) / Fig (e,f). The relative contribution of PAN is highest over East China outflow region, and decrease gradually accompanied with transport.
- For the whole northern hemisphere, the relative contribution of East Asian PAN is about 20% in spring and 10% in summer. The larger relative contribution in spring is mainly because of more East Asia PAN export in spring; and more direct O_3 production over East Asia in summer.

Perturbation Types		Change of O3 over W North America			
		2005-2010 E Asia[a]		2008 E Russia[b]	
		below 800 hPa	800-400hPa	below 800 hPa	800-400hPa
Mar - May	10% NOx change	0.29%	0.43%	0.19%	0.14%
	10% PAN change	0.07%	0.09%	0.10%	0.07%
	PAN role	24%	21%	53%	50%
Jun - Aug	10% NOx change	0.16%	0.37%	0.14%	0.22%
	10% PAN change	0.02%	0.05%	0.04%	0.05%
	PAN role	13%	14%	29%	23%

- Response of O_3 over western North America (122.5-97.5°W, 28-52°N) to Asian NO_x and PAN perturbation.
- Column (a) Multi-year mean change of O_3 due to 10% reduction of East Asian NO_x, PAN and the relative contribution of PAN.
- Column (b) Change of O_3 in 2008 due to 10% reduction of East Russia (97.5-152.5°E, 44-60°N) NO_x, PAN and the relative contribution of PAN.

- The role of boreal Asian biomass burning PAN is about 50% in spring and 20% in summer. The larger contribution is mainly due to the direct conversion from NO_2 to PAN.
- In western North America lower troposphere, the influence from boreal Asian biomass burning in a strong biomass burning year is comparable with that from East Asian emissions.

Summary

- PAN plays a big role in the long-range transport of O_3. The role of East Asian PAN on long-range O3 transport is about 20% in spring and 10% in summer. The seasonal variation is due to the seasonality of East Asian PAN export. The role of boreal Asian biomass burning PAN is about 50% in spring and 20% in summer.
- Asia emissions have important influence on air quality over western North America. The influence from boreal Asian biomass burning in a strong biomass burning year is comparable with that from East Asian emissions.

For more information, please contact: zhe.jiang@jpl.nasa.gov

National Aeronautics and Space Administration
Jet Propulsion Laboratory
California Institute of Technology
Pasadena, California

www.nasa.gov

Poster No. EB-10

National Aeronautics and Space Administration

Exploring spatial and temporal gradients in atmospheric CO_2 and CO using in situ observations in the Los Angeles megacity

Principal Investigator: Kristal R. Verhulst (329L)

Co-Investigators: Francesca Hopkins (329L), Sha Feng (329D), Preeti Rao (329G), Charles Miller (3290), and Riley Duren (8000)

1. Introduction

- Atmospheric carbon dioxide (CO_2) levels have risen globally since the pre-industrial period, correlating with trends in CO_2 emissions from global fossil fuel consumption.
- Cities account for roughly 70% of the fossil fuel carbon dioxide emissions (CO_2ff) and their emissions are spatially and temporally heterogeneous.
- In the future, the number of megacities is expected to increase due to urbanization (from 22 in 2012 to 38 in 2025).
- Therefore, it is necessary to develop robust measurement techniques to resolve CO_2ff emissions in large cities with high spatio-temporal resolution.
- Linking urban atmospheric observations in Los Angeles with fine-scale emissions data will improve our understanding of the relationship between CO_2ff emissions and social, behavioral and economic activities, as well as the effectiveness of emissions control policies.

2. Objectives

(1)Evaluate potential background sites for CO_2 and CO in the LA megacity

(2)Estimate CO_2 and CO enhancements at urban sites in LA relative to background to detect spatiotemporal patterns of CO_2ff

(3)Verify continuous in situ CO(xs)/CO_2(xs) ≈ CO_2-ff^{-1} is a valid proxy for fossil fuel CO_2 emissions via comparisons with $^{14}CO_2$ flask samples

3. Los Angeles In Situ Carbon Monitoring Network

Four tower sites (GH, CP, SCI, and VV)

Three rooftop sites (CSUF, USC, and UCI)

$^{14}CO_2$ flask-sampling underway at 3 LA sites since Fall 2014 (led by NOAA/ESRL); sampling midday, every 3-4 days at Granada Hills, USC and CSUF

CO_2, CO, and CH_4 concentrations tied to the NOAA/WMO scale

LEGEND

Red = Picarro G2401 analyzers (CO_2/CO/CH_4/H_2O)

Blue = Picarro G2301 analyzers (CO_2/CH_4/H_2O)

CIRCLE = TOWER SITE

SQUARE = ROOFTOP SITE

4. Background Site Selection

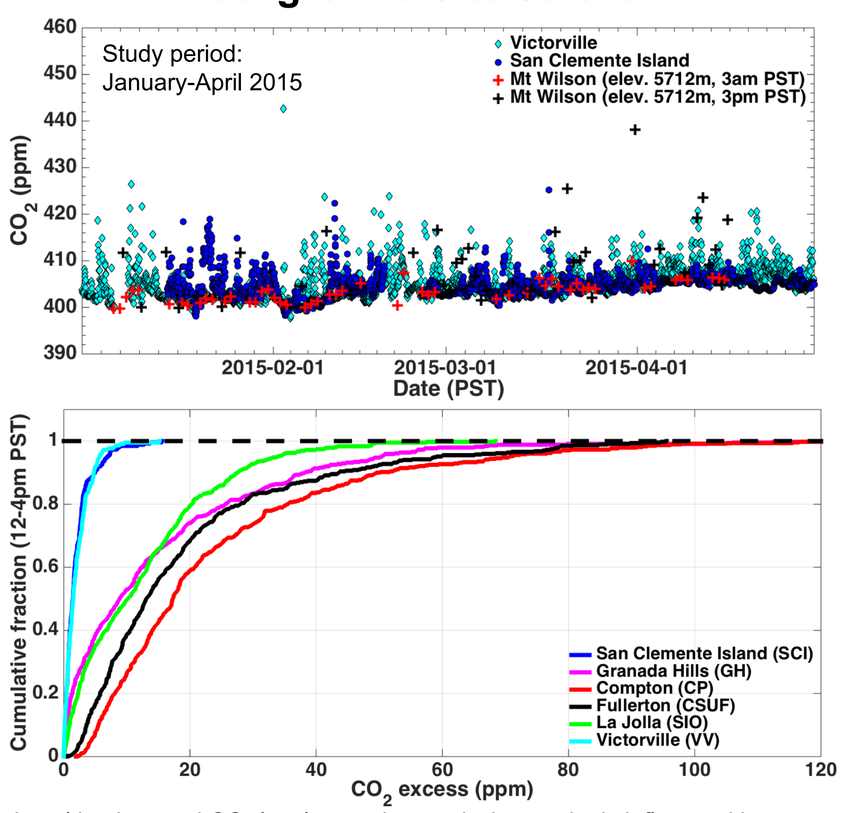

- Local background CO_2 levels are observed when a site is influenced by unpolluted maritime or continental air masses
- San Clemente Island, Victorville, and Mt Wilson typically experience the lowest CO_2 enhancements in the network
- "CO_2 excess" defined as difference between the observed hourly averaged CO_2 mixing ratio and the minimum CO_2 level measured for that hour at all network sites
- San Clemente Island and Victorville show <5 ppm CO_2 excess during roughly 90% of the afternoon hours (12 - 4 pm PST)

5. Diurnal and Spatial Variability of COxs:CO_2xs in the Los Angeles Megacity

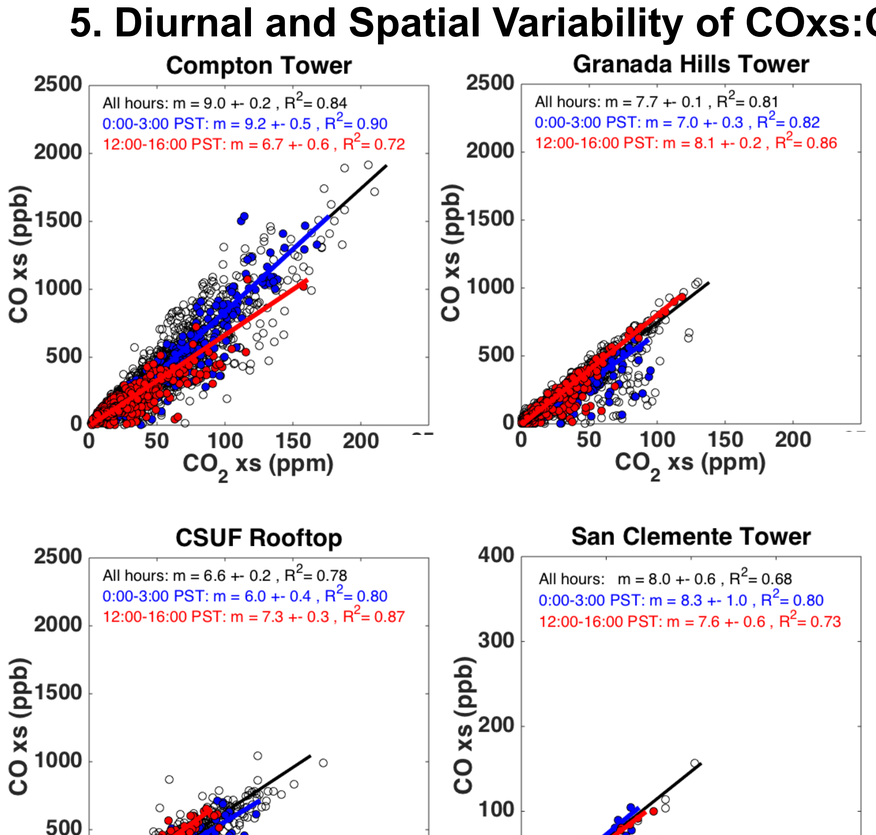

Fossil Fuel CO_2 Estimates for California

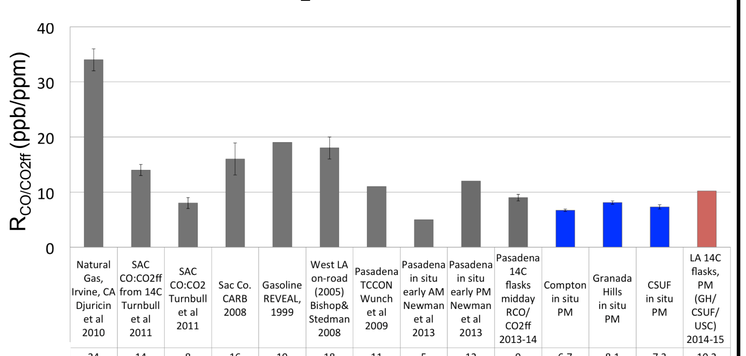

$$R_{CO/CO2} = (CO_2ff)^{-1} = \Delta CO/\Delta CO_2 = CO_{(urb)} - CO_{(bkgd)} / CO_{2(urb)} - CO_{2(bkgd)}$$

- CO is widely used a tracer for CO_2ff; however CO_2 and CO do not have identical sources
- CO_2 concentrations are impacted by FF combustion as well as photosynthesis and respiration, while
- CO is produced from FF combustion and oxidation of anthropogenic and BVOCs
- $R_{CO/CO2}$ depends on fuel source and type (e.g. domestic heating vs traffic), combustion efficiency, etc.

- During Jan-April 2015, Compton, Granada Hills, and CSU Fullerton sites exhibit large urban excess CO_2 and CO signals
- Some difference in the CO excess : CO_2 excess ratio is different at 0:00-3:00 PST and 12:00-4:00 PST
- In situ data exhibit lower slope at midday relative to the CO excess : CO_2ff correlation based on ^{14}C flasks (10.2±0.4 ppb/ppm at roughly 13:00 PST)
- Future work will investigate effects of fires on the use of CO excess : CO_2 excess ratios as tracer of CO_2ff during the study period

Example: Simulated CO_2ff from the WRF-Hestia framework

Hestia Fossil CO_2 Emissions (kg/hr) 9/12/2011 12:00 PST

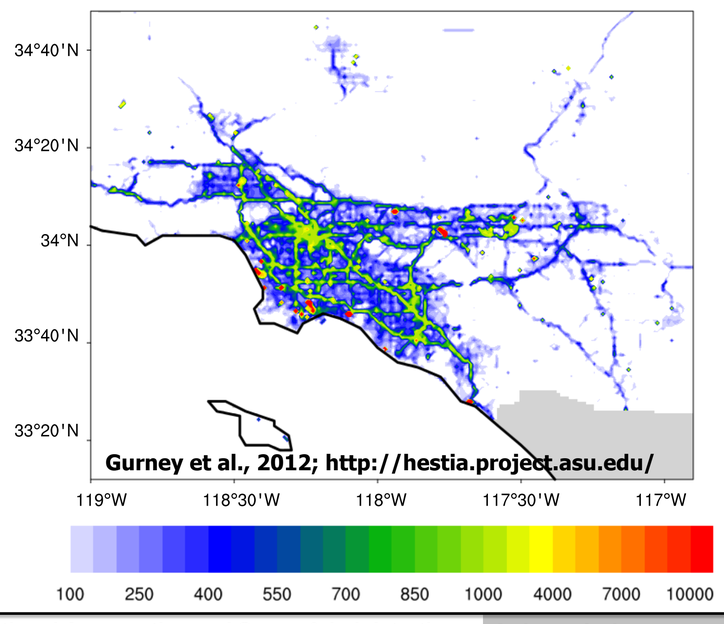

Anthropogenic CO_2 concentrations (ppm) 9/12/2011 12:00 PST (0-16 magl)

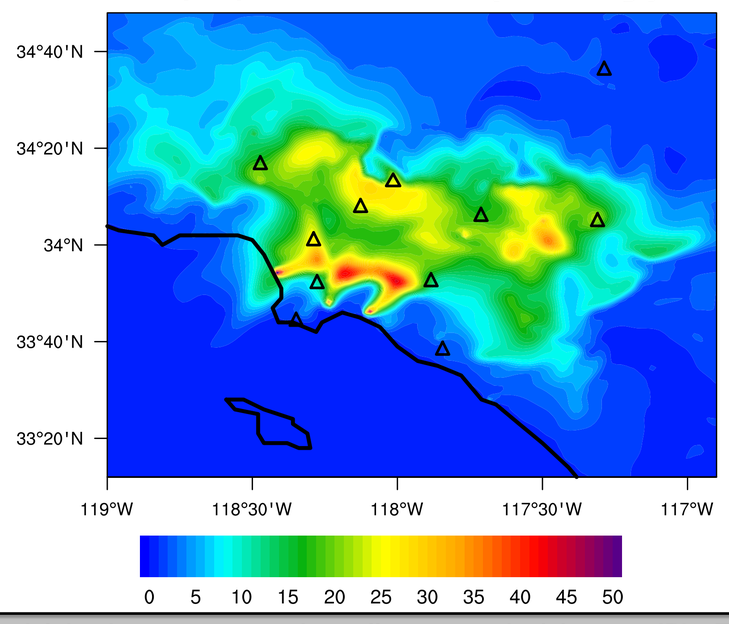

6. Summary and Future Work

Large urban excess CO_2 and CO signals observed at the Compton, Granada Hills and Fullerton sites

Urban sites show variability in the CO excess : CO_2 excess ratio, suggesting variable source mixtures during day/night

Use of CO as a tracer for excess CO_2ff in LA must be validated using diurnal flask measurements of $\Delta^{14}C$. Diurnal 14C flask sampling is planned (summer/winter, measurements roughly every 6 hours)

In future work, CO_2 observations will be compared with a forward simulation WRF-Hestia using the 4km and 1.3 km nested domain – **see Poster #EB-2** for WRF/LA study during the Calnex period, May-June 2010

In future studies, CO_2 enhancements from local sources will be investigated using the tower observations and bottom-up emissions data from the Hestia high-resolution fossil fuel CO_2 inventory

Influence functions for each site will also be generated using high resolution meteorological fields coupled with a LPDM (e.g. WRF-STILT)

National Aeronautics and Space Administration

Jet Propulsion Laboratory
California Institute of Technology
Pasadena, California
www.nasa.gov

Acknowledgements: Special thanks to my supportive colleagues and advisors at JPL. This work would not be possible without technical support for the instrumentation and GCWerks software from Scripps Institution of Oceanography (Ralph Keeling, Ray Weiss, Jooil Kim, and Peter Salameh) and Earth Networks (Amanda Long, Christopher Sloop, and Bill Angel). Government sponsorship acknowledged. This project is jointly funded by the US National Aeronautics and Space Administration (NASA), National Institute of Standards and Technology (NIST) GHG and Climate Science Measurements Program, and National Oceanographic and Atmospheric Administration (NOAA).

Poster No: EB-11

National Aeronautics and Space Administration

Cloud Evolution during the Indian Monsoon Intraseasonal Oscillation: Connection to Large-Scale Dynamics

Principal Investigator: Tao Wang (322)

Co-Is: Sun Wong, Eric J. Fetzer (322)

1. Objective

Establish relationships between cloud regimes and large-scale dynamical states during the Indian Monsoon Intraseasonal oscillation (ISO).

2. Data & Method

- **MODIS**: Clouds τ–CTP

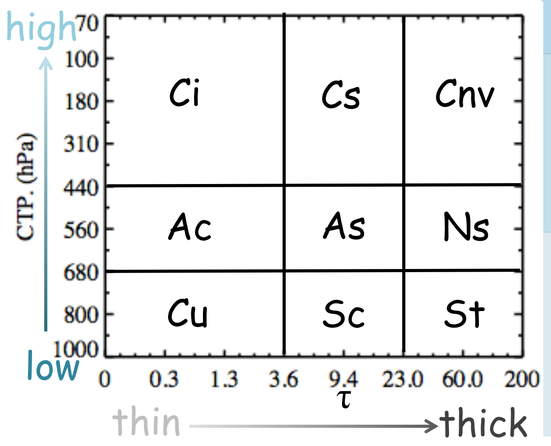

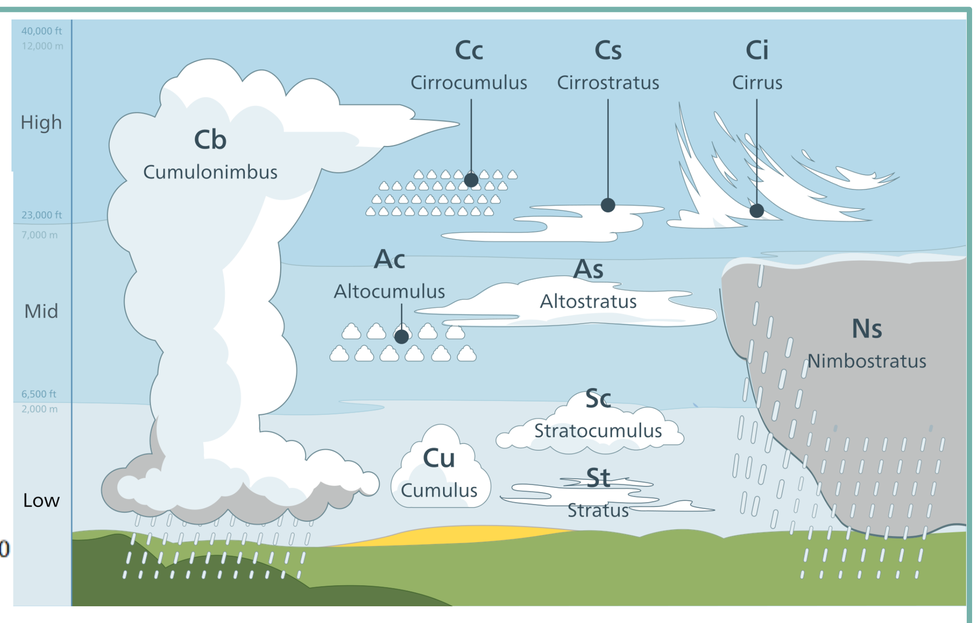

- **MERRA**: approximate water budget (P-E) with large-scale dynamical states

$$P_{recipitation} - E_{vaporation} \approx (-Q\nabla\cdot V) + (-V\cdot\nabla Q) = Qcnvg + Qadvt = Convergence + Advection$$

$$Q = \int_{P_{top}}^{P_{surf}} q\,\frac{dp}{g}\ \textit{column integral of specific humidity} \qquad \vec{V} = \frac{1}{Q}\int_{P_{top}}^{P_{surf}} (\vec{u}\,q)\,\frac{dp}{g}\ \textit{column integral of water flux (weighted by Q)}$$

- **GPCP**: monsoon precipitation as ISO indices

GPCP Precipitation over Indian Monsoon (**70-90°E, 10-25°N**): 10-90 day FFT filtering

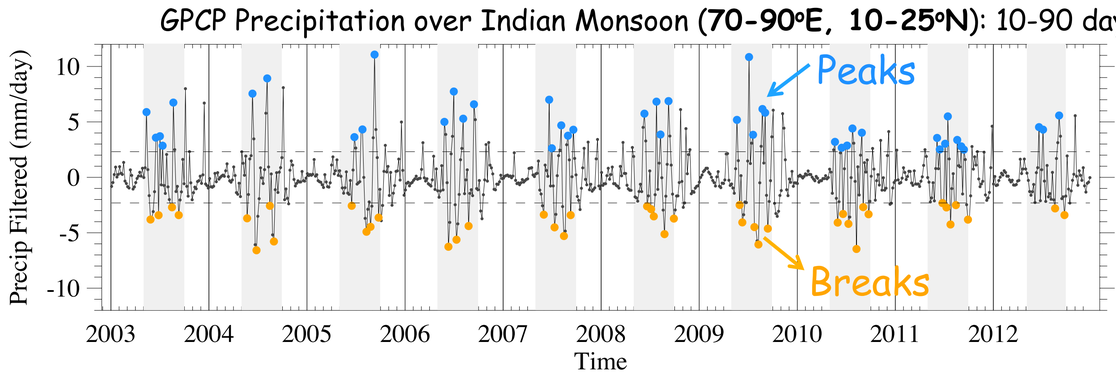

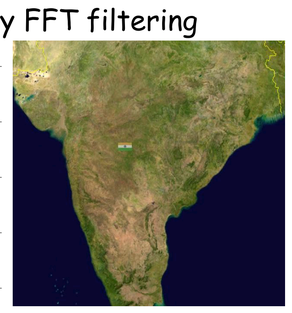

Summary: study **Clouds** in responses to [*Qcnvg* *Qadvt*] during ISO

3. Results: overview

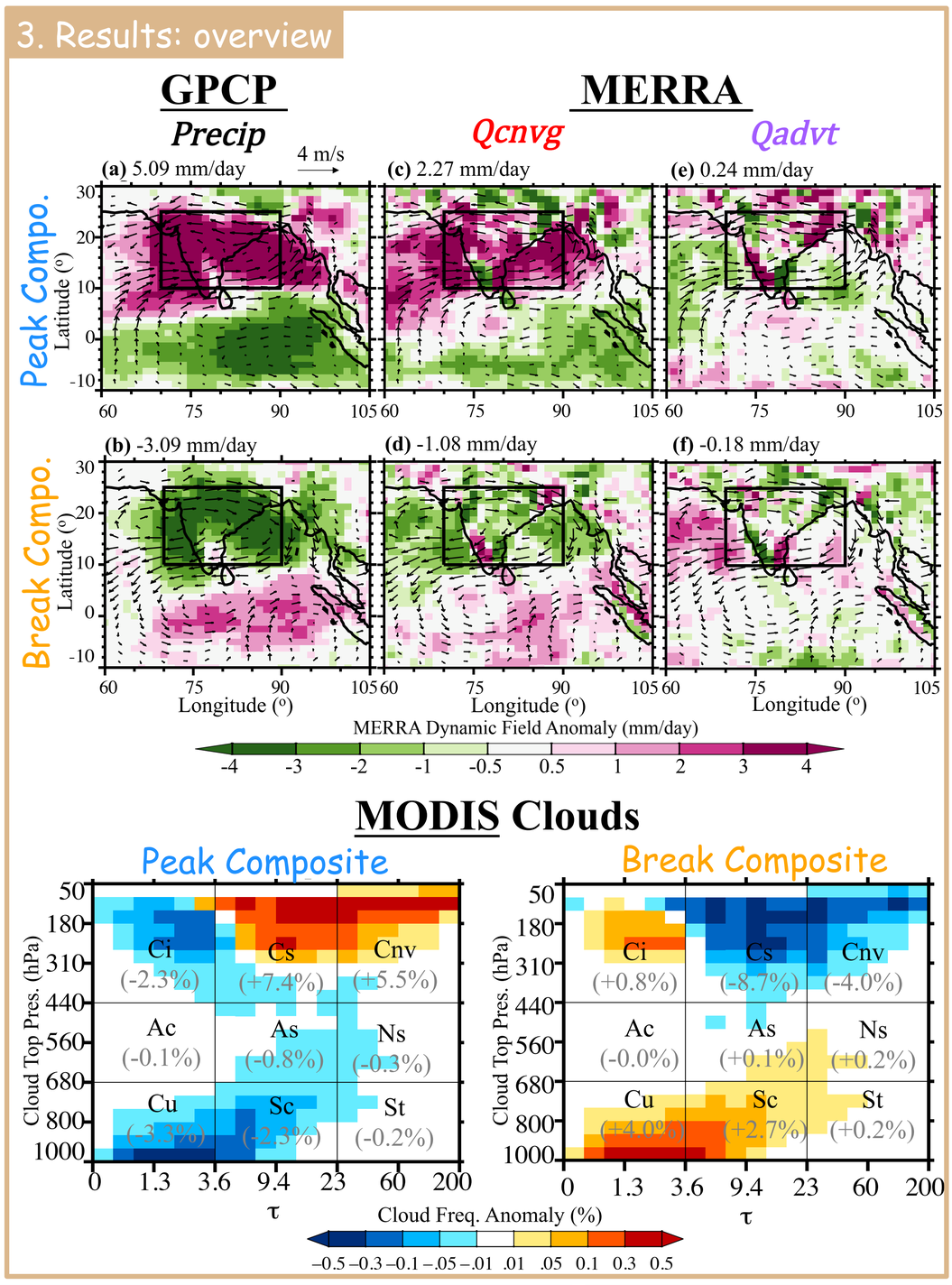

MODIS Clouds

4. Dynamical & Cloud Evolutions

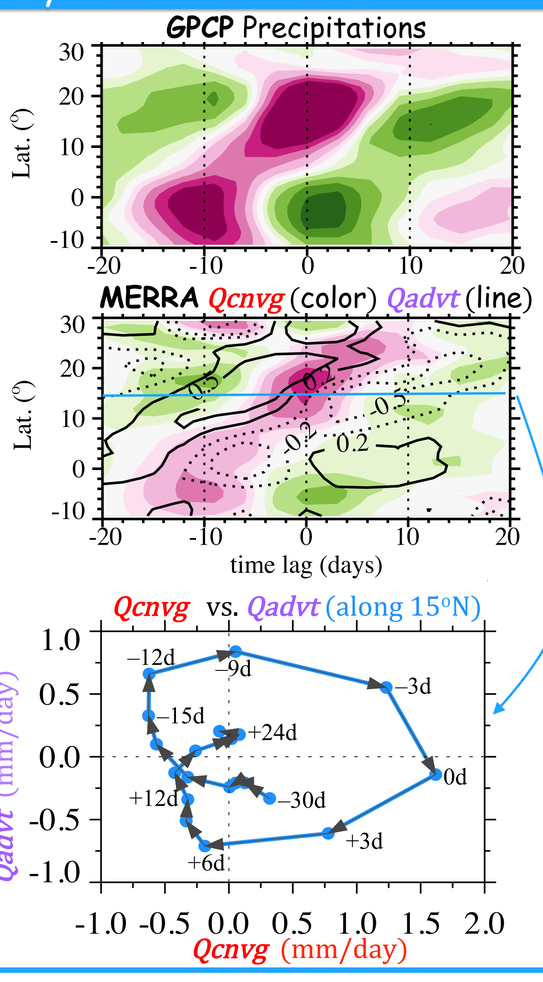

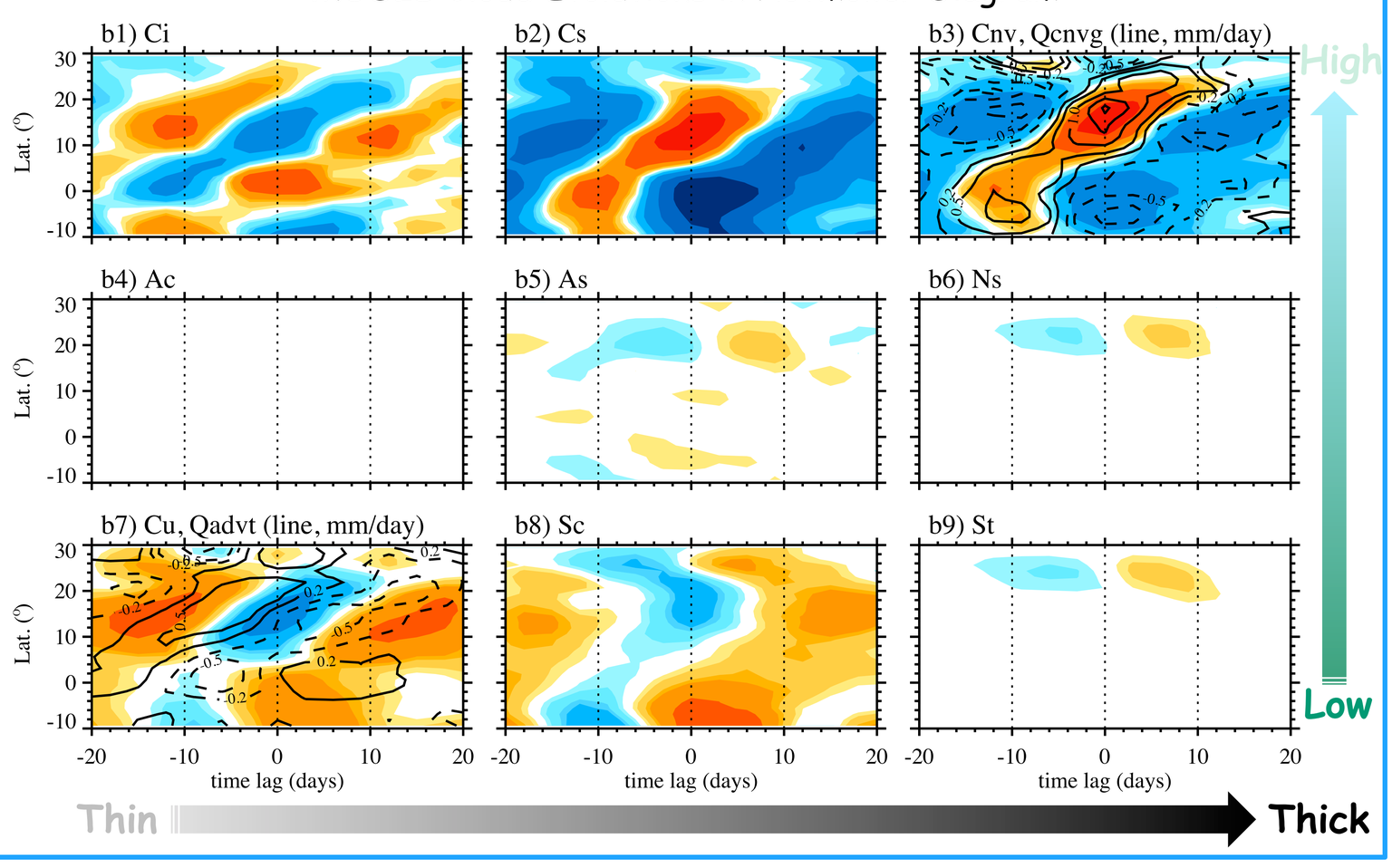

5. Summary

- Moisture convergence (*Qcnvg*) and moisture advection (*Qadvt*) represents total water budget very well;
- **Strong coupling** as well as mutual reinforcing and hindering **of clouds to dynamical states**;
- MODIS **Cnv** and **Cs** are strongly associated with *Qcnvg*; whereas MODIS **Cu** and **Sc** are associated with moisture *Qadvt*;
- *Qadvt* leads *Qcnvg* 3-4 days: low level pre-conditioning in favor of transitions from **Cu**/**St** to **Cnv**;
- **Ci** over land resembles **Cu**, but over ocean is more frequent, likely due to equatorial wave perturb.;
- No obvious variations of middle clouds **Ac**, probably due to MODIS retrieval issues on broken clouds.

National Aeronautics and Space Administration

Jet Propulsion Laboratory
California Institute of Technology
Pasadena, California
www.nasa.gov

Poster No. EB-12

National Aeronautics and Space Administration

Physics-based Modeling of Ionospheric Signatures Induced by Tsunamis

Xing Meng (335G, xing.meng@jpl.nasa.gov), Attila Komjathy (335G), Olga P. Verkhoglyadova (335G), Yu-Ming Yang (335G), Yue Deng (UT-Arlington), and Anthony J. Mannucci (335G)

1. Introduction

Background: Tsunamis can generate upward-propagating atmospheric gravity waves, inducing electron density perturbations that can be observed in the ionosphere. Ionosphere monitoring might detect tsunamis before they arrive at coastlines.

Motivation: Modeling tsunami-induced ionospheric signatures can aid in understanding observations and the tsunami-ionosphere coupling. However, previous models either rely on an empirical atmospheric and ionospheric background that lacks self-consistent coupling between neutrals and ions or neglect some physical processes and space weather effects in the upper atmosphere, which limits the modeling ability to represent reality.

Objective: Develop a **time-dependent**, **three-dimensional**, and **physics-based** tsunami-ionosphere model to overcome the limitations of previous models and better capture the ionospheric signatures induced by tsunamis.

2. Model description

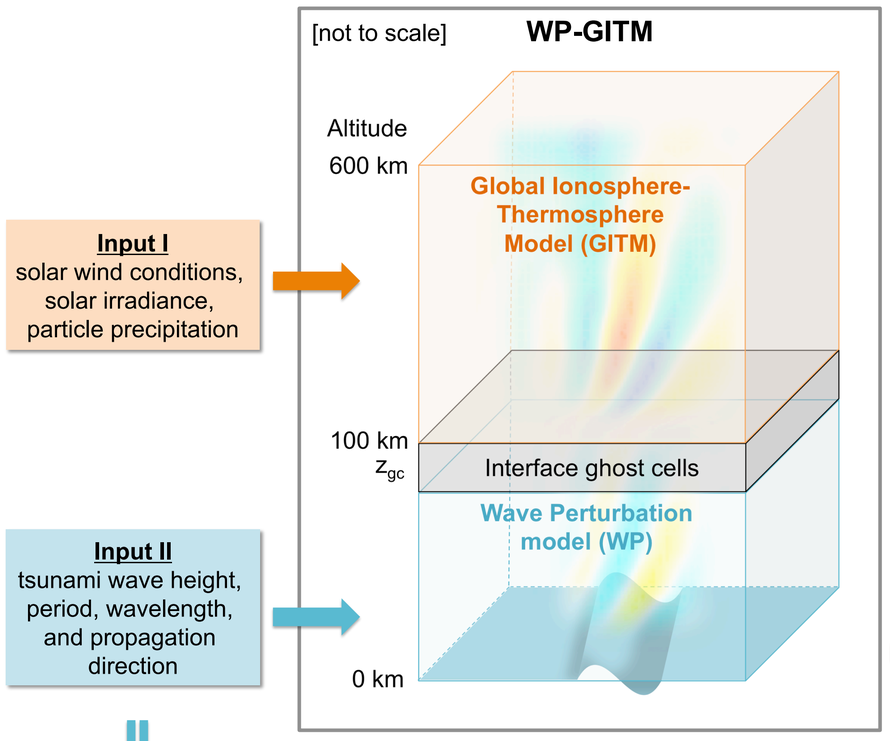

Key features of Wave Perturbation – Global Ionosphere-Thermosphere Model (WP-GITM)

- analytical model WP (0 km – 100 km altitudes) + physics-based model GITM (100 km – 600 km altitudes)
- 10 neutral and 9 ion species
- includes a rich variety of physical processes in the upper atmosphere: chemical reactions, viscosity, heat conduction, radiative cooling, ion-neutral and neutral-neutral collisions, geomagnetic field and earth's rotation
- includes space weather effects: solar extreme ultraviolet heating, auroral particle precipitation, high-latitude electric field
- flexible computational domain and grid resolution

3. Event simulation

The 11 March 2011 Tohoku-Oki tsunami waves propagated across the Pacific Ocean, inducing ionospheric perturbations over the US west coast.

Simulated local region:
US west coast

Simulated time period:
14:45 UT – 20:45 UT

Tsunami characteristics
from the Method of Splitting model (only consider the most significant waves):

Period = 20 minutes
Wavelength = 150 km
Wave A height = 8 cm
Wave B height = 10 cm
Wave C height = 9 cm

Tsunami waves at the ocean surface and neutral perturbations at the interface

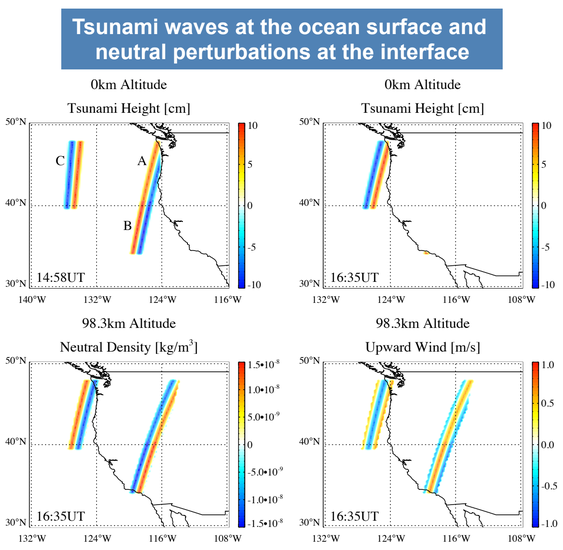

Simulated density perturbations

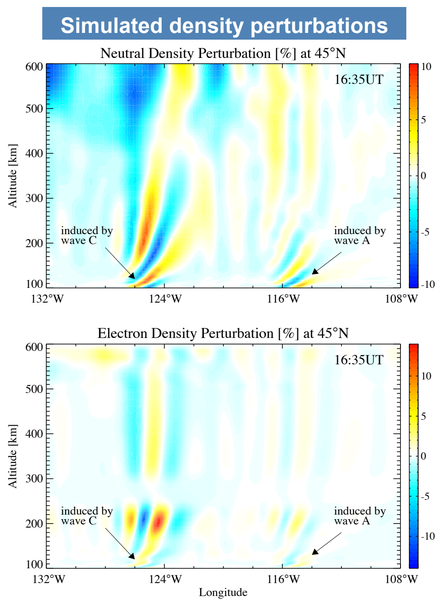

Two simulations with and without tsunami waves are performed. The differences between the two simulation results are ionospheric disturbances due to the tsunami.

Neutral and electron density perturbations: strong responses (~10%) to tsunami wave C and weaker responses (~5%) to tsunami wave A.

4. Validation

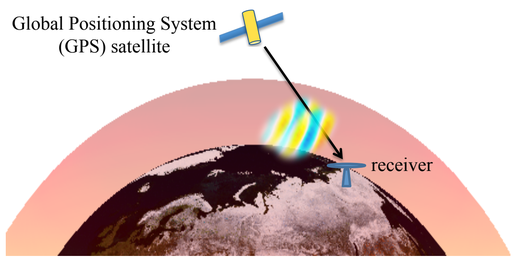

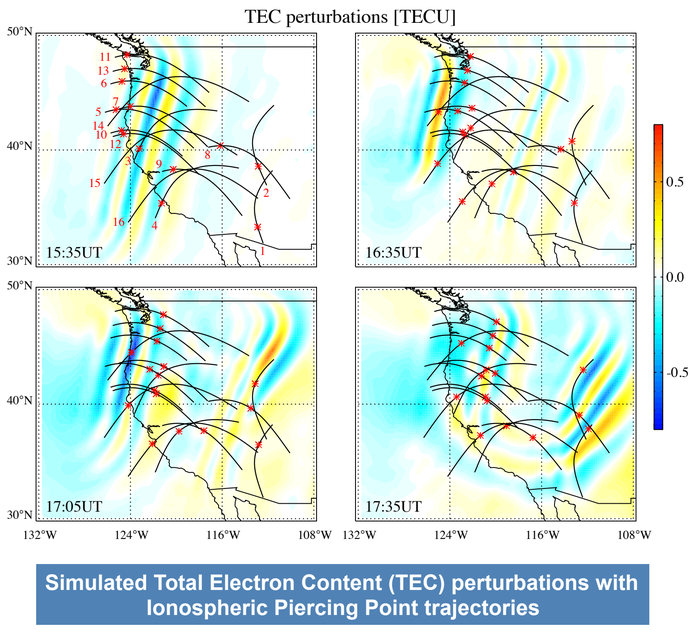

Simulated Total Electron Content (TEC) perturbations with Ionospheric Piercing Point trajectories

Comparison with GPS observations

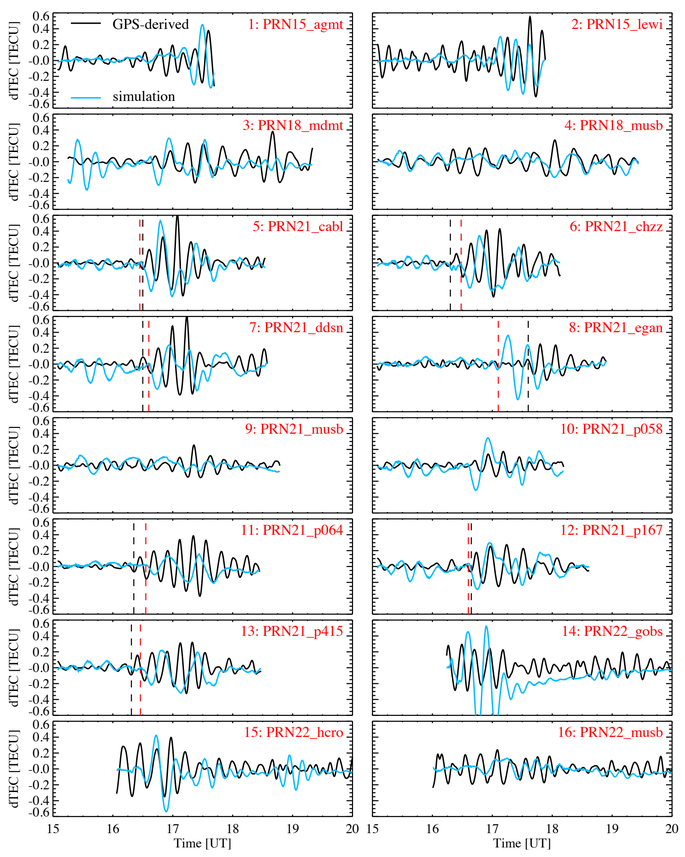

5. Conclusions

Originality: We have successfully developed a self-consistent physics-based model WP-GITM that simulates tsunami-caused upper atmospheric disturbances. With WP-GITM, the GPS-observed travelling ionospheric signatures of an actual tsunami event have been reproduced **for the first time**.

Possible reasons for model-data disagreement:

- limitations of the analytical wave perturbation model (constant temperature, etc.);
- the simplification of the input tsunami waves;
- uncertainties in GPS-derived TEC perturbations.

6. Future work & Applications

- Study model limitations and refine WP-GITM.
- Include acoustic waves to model ionospheric signatures due to earthquakes and volcanic eruptions.
- **Application I**: detection and/or early warnings of natural hazards such as tsunamis, earthquakes, and volcanic eruptions.

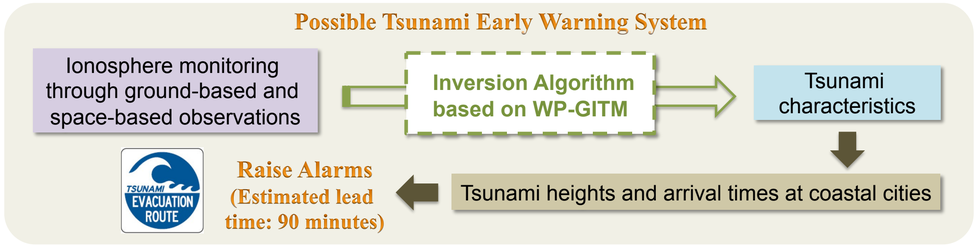

- **Application II**: planetary seismology including remote sensing of Venusian atmosphere and ionosphere.

National Aeronautics and Space Administration
Jet Propulsion Laboratory
California Institute of Technology
Pasadena, California

www.nasa.gov

Acknowledgement

- NASA ROSES NNH10ZDA001N-GEOIM and NNH10ZDA001N-ESI for funding this research;
- J. H. King, N. Papatashvilli at AdnetSystems, NASA GSFC, and CDAWeb for providing the solar wind data;
- The Plate Boundary Observation network for the GPS data;
- JPL high-performance computing.

Poster No. EB-13

National Aeronautics and Space Administration

Uncertainty Quantification for the Orbiting Carbon Observatory-2: Surrogate Model Monte Carlo Experiments

Investigator: Jonathan Hobbs (398L)
Amy Braverman (398L), Noel Cressie (University of Wollongong), Robert Granat (398J), Michael Gunson (8020), Hai Nguyen (398L)

Monte Carlo Framework

- Monte Carlo simulation (Figure 1) can quantify the impact of algorithm design choices and additional sources of uncertainty on X_{CO2} retrieval *bias* and *covariance*.
- A physically-based surrogate model and optimal estimation retrieval, $R(\mathbf{Y}_2,\mathbf{B}_0)$, captures key sources of uncertainty while ensuring computational efficiency.

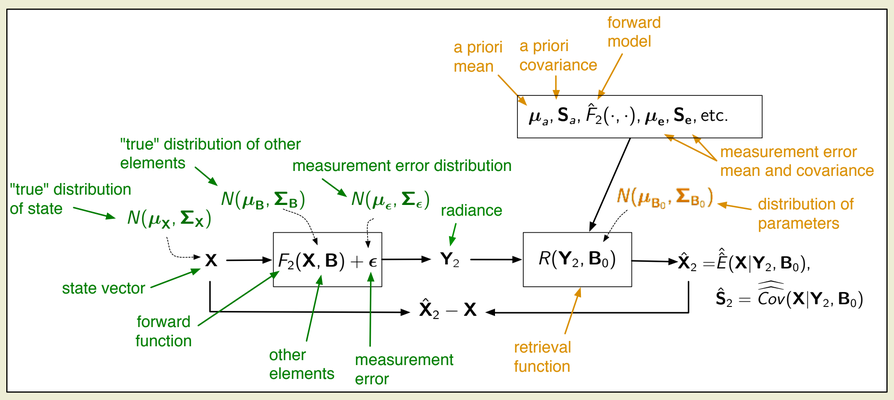

Retrieval Error:

$$\boldsymbol{\Delta} = \hat{\mathbf{X}}_2 - \mathbf{X}$$

Figure 1. Surrogate model and retrieval simulation framework. Elements in green are known, and elements in orange represent retrieval algorithm choices.

Uncertain Retrieval Inputs

- **Objective**: Decompose retrieval error ($\boldsymbol{\Delta}$) variance into contribution from uncertainty about the prior mean and contribution from variability in **X** and **Y**.
- A hierarchical sampling approach is used. Albedo and aerosol prior means are randomly sampled, with a small Monte Carlo experiment for each prior mean.
- **Key finding**: Both variance components contribute comparably, differing slightly by aerosol type (Figure 2).

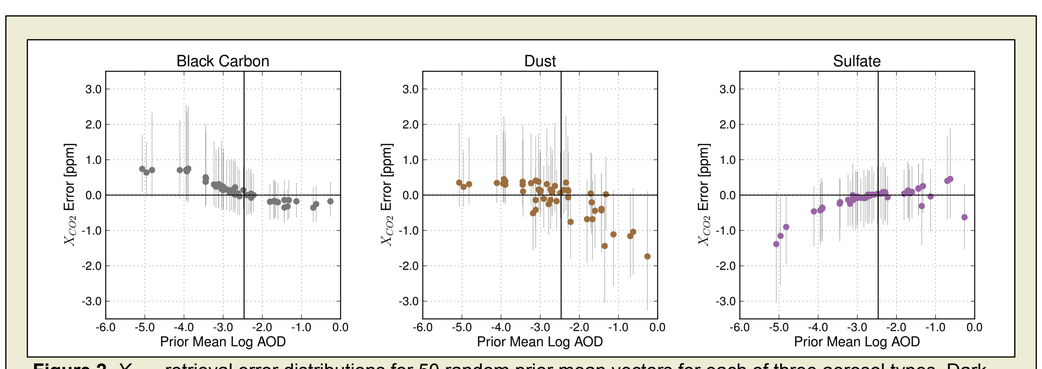

Figure 2. X_{CO2} retrieval error distributions for 50 random prior mean vectors for each of three aerosol types. Dark vertical line depicts the true marginal mean log AOD. Points depict the mean retrieval error, and thin vertical lines enclose the center 95% of the error distribution within each prior mean.

Variance Component		Black Carbon	Dust	Sulfate
Across prior means [ppm²]	$Var(E(\boldsymbol{\Delta}\|\boldsymbol{\mu}_a))$	0.099	0.259	0.110
Within a prior mean [ppm²]	$E(Var(\boldsymbol{\Delta}\|\boldsymbol{\mu}_a))$	0.175	0.282	0.190

Prior Mean Sensitivity

- **Objective:** Quantify the impact of systematic misspecification of albedo and aerosol prior mean on retrieval error (Table 1).

$$\boldsymbol{\mu}_a = \boldsymbol{\mu}_{\mathbf{X}} + \boldsymbol{\delta}$$

Aerosol \ O_2 Albedo	$\boldsymbol{\delta}$	$-\sigma_{\mathbf{X}}$	**0**	$\sigma_{\mathbf{X}}$
	$-\sigma_{\mathbf{X}}$	N_N	N_O	N_P
	0	O_N	O_O	O_P
	$\sigma_{\mathbf{X}}$	P_N	P_O	P_P

Table 1. Conditions for the prior mean misspecification experiment. Rows represent the log AOD prior mean, and columns represent the O_2 A-band albedo prior mean.

Additional Factors

Location/Geophysical state
- High aerosol optical depth
- Low aerosol optical depth

Aerosol type
- Black carbon (BC)
- Dust (DU)
- Sulfate (SO)

- **Key finding:** Aerosol prior mean misspecification can impact X_{CO2} retrieval bias, but retrieval is more robust in low aerosol conditions (Figure 3).

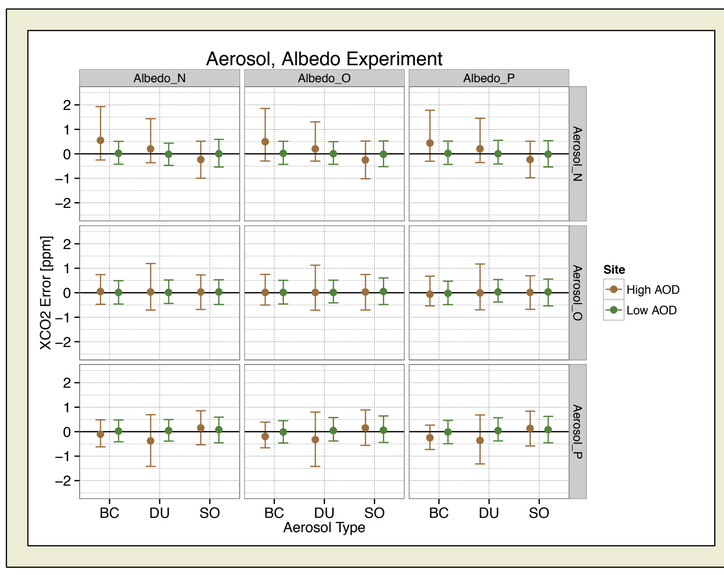

- AOD prior mean impacts retrieval error more critically than A-band albedo.
- Aerosol type impacts both bias and variance.

Figure 3. X_{CO2} retrieval error distribution for combinations of aerosol and albedo prior mean misspecification. Points depict the mean retrieval error (bias), and error bars enclose the center 95% of the error distribution.

- Actual error variance can be larger than the retrieval's reported posterior variance for certain aerosol types (Figure 4).

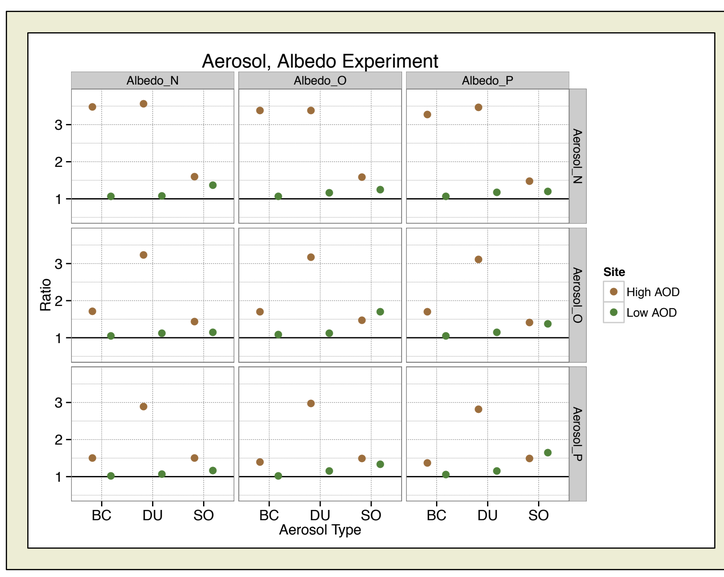

- Optimal estimation retrieval provides an approximate retrieval posterior covariance.
- Simulations suggest this can be an underestimate in high AOD conditions for some aerosol types.

Figure 4. Ratio of X_{CO2} error standard deviation to the reported retrieval standard deviation for combinations of aerosol and albedo prior mean misspecification.

National Aeronautics and Space Administration
Jet Propulsion Laboratory
California Institute of Technology
Pasadena, California

www.nasa.gov

Poster No. EB-14